Petroleum Science 20 (2023) 2060–2074

Contents lists available at ScienceDirect

Petroleum Science

journal homepage: www.keaipublishing.com/en/journals/petroleum-science

Original Paper

# Fast pre-stack multi-channel inversion constrained by seismic reflection features

Ya-Ming Yang [a, b, c], Xing-Yao Yin [a, b, c, *], Kun Li [a, b, c], Feng Zhang [d], Jian-Hu Gao [e]

[a] School of Geosciences, China University of Petroleum (East China), Qingdao, Shandong, 266580, China
[b] Pilot National Laboratory for Marine Science and Technology (Qingdao), Qingdao, Shandong, 266580, China
[c] Shandong Provincial Key Laboratory of Deep Oil and Gas, Qingdao, Shandong, 266580, China
[d] China University of Petroleum-Beijing, Beijing, 102249, China
[e] Research Institute of Petroleum Exploration and Development-Northwest, Lanzhou, Gansu, 730020, China

ARTICLE INFO

*Article history:*
Received 21 February 2022
Received in revised form
21 November 2022
Accepted 14 February 2023
Available online 16 February 2023

Edited by Jie Hao

*Keywords:*
Pre-stack multi-channel inversion
Reflection features
Fast optimization

ABSTRACT

Classical multi-channel technology can significantly reduce the pre-stack seismic inversion uncertainty, especially for complex geology such as high dipping structures. However, due to the consideration of complex structure or reflection features, the existing multi-channel inversion methods have to adopt the highly time-consuming strategy of arranging seismic data trace-by-trace, limiting its wide application in pre-stack inversion. A fast pre-stack multi-channel inversion constrained by seismic reflection features has been proposed to address this issue. The key to our method is to re-characterize the reflection features to directly constrain the pre-stack inversion through a Hadamard product operator without rearranging the seismic data. The seismic reflection features can reflect the distribution of the stratum reflection interface, and we obtained them from the post-stack profile by searching the shortest local Euclidean distance between adjacent seismic traces. Instead of directly constructing a large-size reflection features constraint operator advocated by the conventional methods, through decomposing the reflection features along the vertical and horizontal direction at a particular sampling point, we have constructed a computationally well-behaved constraint operator represented by the vertical and horizontal partial derivatives. Based on the Alternating Direction Method of Multipliers (ADMM) optimization, we have derived a fast algorithm for solving the objective function, including Hadamard product operators. Compared with the conventional reflection features constrained inversion, the proposed method is more efficient and accurate, proved on the Overthrust model and a field data set.


## 1. Introduction

Pre-stack seismic inversion focuses on the amplitude variation with offset or angle (AVO/AVA) and aims to quantitatively evaluate the lithologic and fluid properties of the subsurface media from the observed data (Smith and Gidlow, 1987; Yin et al., 2015; Zong et al., 2013, 2015, 2017; Li et al., 2020, 2021). P-wave and S-wave are two types of vibrations that geophysicists have been interested in because of their different responses to the rock matrix and fluid types (Goodway et al., 1997; Gray and Andersen, 2000; Zhang et al., 2015). The P-, S-wave information can be obtained by inverting the pre-stack seismic data since the AVO or AVA analysis is related to P-velocity, S-velocity, and density on both sides of a layer interface (Aki and Richards, 1980; Wang et al., 2019; Xi et al., 2022). For this reason, pre-stack seismic inversion has been widely studied and applied in hydrocarbon exploration (Zhang et al., 2011; Rimstad et al., 2012; Zong et al., 2021). However, seismic inversion is an ill-posed problem with substantial uncertainty. Moreover, the continuity and fidelity of the inversion model in complex geology are essential factors that affect the quantitative interpretation of reservoirs. Several studies have shown that the existing multi-channel seismic inversion can effectively deal with these issues (Zhang et al., 2013b; Yuan et al., 2015).

Different from the conventional trace-by-trace processing

*Abbreviations:* ADMM, the Alternating Direction Method of Multipliers; SCI, structurally constrained inversion.

* Corresponding author. School of Geosciences, China University of Petroleum (East China), Qingdao, Shandong, 266580, China.
*E-mail address:* xyyin@upc.edu.cn (X.-Y. Yin).

https://doi.org/10.1016/j.petsci.2023.02.009

technology, multi-channel technology is a simultaneous optimization strategy for 2D/3D seismic datasets that can process multiple or all seismic traces simultaneously and consider the relationship between adjacent seismic traces. Due to the excellent performance in noise suppression and continuity, especially for complex geology, the multi-channel technology has been widely studied in the fields of denoising (Abma and Claerbout, 1995), seismic processing (Liu et al., 2009; Zhang and Alkhalifah, 2019), and seismic inversion (Li et al., 2018; Cheng et al., 2020). Among them, seismic multi-channel inversion has been paid more and more attention in recent years. The primary multi-channel inversion does not consider the lateral constraints, known as laterally unconstrained inversion (1D-LUI) (Hamid and Pidlisecky, 2015). It can usually obtain a higher quality profile by inverting the multiple seismic gathers simultaneously, compared to the conventional single trace inversion (Kazemi and Sacchi, 2014; Nose-Filho et al., 2015; Ma et al., 2018). However, it may produce a discontinuous model because it does not consider the lateral distribution of the stratum (Zhang et al., 2013a, 2013b). To deal with this issue, Zhang et al. (2013b) and Hamid and Pidlisecky (2015) proposed the laterally constrained inversion (1D-LCI), assuming that the stratum is horizontally distributed (Hamid and Pidlisecky, 2015). In general, the lateral continuity can be controlled by regularizing the first or second partial derivatives of the model parameters along the horizontal direction (Sroubek and Milanfar, 2012). As we know, the prior constraints are suboptimal when assumptions do not match reality. The 1D-LCI method may produce ambiguous boundaries if the stratum is not horizontally distributed, such as faults and high dipping structures (Hamid and Pidlisecky, 2016; Bai et al., 2019). To overcome this problem, constructing reasonable constraints more in line with stratum structure has gradually become the focus of multi-channel inversion research (Hamid et al., 2018; Yin et al., 2020). At present, two mainstream strategies can construct a reasonable structural prior. One is to describe the structure characteristics by dip angles estimated from the migrated dataset, represented by the structurally constrained inversion (SCI) (Hamid and Pidlisecky, 2016; Hamid et al., 2018; Cheng et al., 2020). The other describes the seismic reflection events based on correlation analysis, represented by reflection features constrained inversion (Yu et al., 2020). It has been widely studied in deconvolution (Du et al., 2018) and absorption compensation (Ma et al., 2020).

However, due to the high computational cost, the SCI and reflection features constrained inversion are challenging to be widely used in practical production, especially for pre-stack inversion. The main reason for the high inversion cost is that the operators describing the stratum structures or seismic reflection events are usually complex, and a dimensionality reduction strategy is required to introduce them into the objective function. This dimensionality reduction strategy arranges the seismic traces into a column vector trace-by-trace, significantly exacerbating the matrix size of the forward operator and constraint operators. Moreover, it is worth noting that the matrix size would increase geometrically with expanding the number of seismic traces, and handling the large-scale matrices is extremely time-consuming. The Block Coordinate Descent (BCD) algorithm was developed gradually to overcome the problem that the inversion is difficult to implement while the number of seismic traces reaches a certain level (Bertsekas, 1999; Wright, 2015; Lee et al., 2017). It approximates the optimal global solution with the optimal local solution of each trace through several iterations. This algorithm dramatically liberates the consumption of computer memory (Wang et al., 2018) but at the expense of computational efficiency. Furthermore, the estimated inversion parameters are not globally optimal. In contrast, the classical total variation (TV) regularization multi-channel inversion is extremely efficient (Gholami and Sacchi, 2013; Gholami, 2015, 2016), belonging to 1D-LCI. It does not adopt the dimensionality reduction strategy because of the simple assumption that the stratum is horizontally distributed. As mentioned, this method always suffers boundary ambiguity for high dip structures. For the current techniques, adopting reasonable prior constraints would reduce efficiency. It seems that the rationality constraints and inversion efficiency cannot be taken into account simultaneously.

We developed a novel method to characterize seismic reflection features by decomposing them into horizontal and vertical directions. To avoid the conventional strategy of seismic trace rearrangement, we use a particular matrix operator, the Hadamard operator, in constructing the regularization terms of reflection features, which represents the product of the corresponding elements of two matrices of the same size. The key is that each matrix element is controllable when the Hadamard product operator operates, which can overcome the complexity of the reflection feature operator. Although the application of this operator in seismic exploration is rare, it plays an irreplaceable role in our method. The difficulty is to minimize the objective function containing the Hadamard product operators. Based on the ADMM strategy, we derived a fast reflection features constrained inversion algorithm called FRCI. This work will first introduce the pre-stack multi-channel forward model based on the Aki-Richards equation. Next, a fast reflection feature constrained inversion is derived according to the classical multi-channel inversion with the BCD algorithm. Finally, the overthrust model and a field data set are adopted to test the feasibility and effectiveness of the proposed approach.

## 2. Pre-stack multi-channel forward modeling

In a pre-stack inversion, the relationship between the PP reflectivity at the layer interfaces and the incident angles, the P-wave velocity, S-wave velocity and density on both sides can be characterized as follows (Aki and Richards, 1980):

$$R_{PP}(\theta) = \sec^2(\theta)R_P - 8\gamma^2 \sin^2(\theta)R_S + \left(1 - 4\gamma^2 \sin^2(\theta)\right)R_\rho \tag{1}$$

where $\theta$ is the incident angle and $\gamma$ is the ratio of average S- and P-velocity at the layer interfaces. The specific forms of reflectivities of the P- and S-wave velocities, and density ($R_P$, $R_S$, and $R_\rho$) can be expressed as follows:

$$R_P^i = \frac{V_P^{i+1} - V_P^i}{V_P^{i+1} + V_P^i} \approx \frac{1}{2}\frac{\Delta V_P^i}{V_P^i} = \frac{1}{2}\Delta \ln V_P^i = \frac{1}{2}\left(\ln V_P^{i+1} - \ln V_P^i\right)$$

$$R_S^i = \frac{V_S^{i+1} - V_S^i}{V_S^{i+1} + V_S^i} \approx \frac{1}{2}\frac{\Delta V_S^i}{V_S^i} = \frac{1}{2}\Delta \ln V_S^i = \frac{1}{2}\left(\ln V_S^{i+1} - \ln V_S^i\right)$$

$$R_\rho^i = \frac{\rho^{i+1} - \rho^i}{\rho^{i+1} + \rho^i} \approx \frac{1}{2}\frac{\Delta \rho^i}{\rho^i} = \frac{1}{2}\Delta \ln \rho^i = \frac{1}{2}\left(\ln \rho^{i+1} - \ln \rho^i\right) \tag{2}$$

where $V_P^i$, $V_S^i$, and $\rho^i$ are the P- and S-wave velocities, and density between the $i^{\text{th}}$ and $(i+1)^{\text{th}}$ layer interfaces, respectively. Further, we can rewrite Eq. (2) in a matrix-vector form:

$$\mathbf{R}_{\mathrm{P}} \approx \frac{1}{2}\mathbf{D}\ln(\mathbf{V}_{\mathrm{P}}) = \frac{1}{2}\mathbf{D}\mathbf{L}_{\mathrm{P}}$$

$$\mathbf{R}_{\mathrm{S}} \approx \frac{1}{2}\mathbf{D}\ln(\mathbf{V}_{\mathrm{S}}) = \frac{1}{2}\mathbf{D}\mathbf{L}_{\mathrm{S}}$$

$$\mathbf{R}_\rho \approx \frac{1}{2}\mathbf{D}\ln(\boldsymbol{\rho}) = \frac{1}{2}\mathbf{D}\mathbf{L}_\rho \tag{3}$$

where $\mathbf{L}_\mathrm{P}$, $\mathbf{L}_\mathrm{S}$, and $\mathbf{L}_\rho$ are the natural logarithms of the $\mathbf{V}_\mathrm{P}$, $\mathbf{V}_\mathrm{S}$ and $\boldsymbol{\rho}$. For a seismic trace containing $m$ sampling points, the first-order difference matrix $\mathbf{D}$ has the following form:

$$\mathbf{D} = \begin{bmatrix} -1 & 1 & 0 & \cdots & 0 \\ 0 & -1 & 1 & \cdots & 0 \\ \vdots & \vdots & \ddots & \ddots & \vdots \\ 0 & 0 & \cdots & -1 & 1 \end{bmatrix}_{m\times(m+1)} \tag{4}$$

Based on Eq. (1), the pre-stack angle gathers ($\overline{\mathbf{S}}(\theta)$) can be obtained by multiplying the reflectivity and the wavelet matrix ($\mathbf{W}(\theta)$).

$$\overline{\mathbf{S}}(\theta) = \frac{1}{2}c_1(\theta)\mathbf{W}(\theta)\mathbf{D}\mathbf{L}_\mathrm{P} + \frac{1}{2}c_2(\theta)\mathbf{W}(\theta)\mathbf{D}\mathbf{L}_\mathrm{S} + \frac{1}{2}c_3(\theta)\mathbf{W}(\theta)\mathbf{D}\mathbf{L}_\rho \tag{5}$$

where $\overline{\mathbf{S}}(\theta)\in\mathbb{R}^{m\times n}$ is the angle-dependent seismic data; $c_1(\theta) = \frac{1}{2}\sec^2(\theta)$, $c_2(\theta) = -4\gamma^2\sin^2(\theta)$, $c_3(\theta) = \frac{1}{2}(1-4\gamma^2\sin^2(\theta))$. $\mathbf{W}(\theta)\in\mathbb{R}^{m\times m}$ is obtained by time-shifting the seismic wavelet as follows:

$$\mathbf{W}(\theta) = \begin{bmatrix} w^1(\theta) & & & \\ w^2(\theta) & w^1(\theta) & & \\ \vdots & w^2(\theta) & \ddots & \\ w^l(\theta) & \vdots & \ddots & w^1(\theta) \\ & w^l(\theta) & \ddots & w^2(\theta) \\ & & \ddots & \vdots \\ & & & w^l(\theta) \end{bmatrix} \tag{6}$$

where $l$ is the length of the seismic wavelet. According to Eq. (5), the matrix form of seismic gathers varying with $\theta$ can be expressed as follows:

$$\underbrace{\begin{bmatrix} \overline{\mathbf{S}}(\theta_1) \\ \overline{\mathbf{S}}(\theta_2) \\ \vdots \\ \overline{\mathbf{S}}(\theta_h) \end{bmatrix}}_{\mathbf{S}} = \underbrace{\frac{1}{2}\begin{bmatrix} c_1(\theta_1)\mathbf{W}(\theta_1)\mathbf{D} & c_2(\theta_1)\mathbf{W}(\theta_1)\mathbf{D} & c_3(\theta_1)\mathbf{W}(\theta_1)\mathbf{D} & c_1(\theta_2)\mathbf{W}(\theta_2)\mathbf{D} & c_2(\theta_2)\mathbf{W}(\theta_2)\mathbf{D} & c_3(\theta_2)\mathbf{W}(\theta_2)\mathbf{D} & \cdots & c_1(\theta_h)\mathbf{W}(\theta_h)\mathbf{D} & c_2(\theta_h)\mathbf{W}(\theta_h)\mathbf{D} & c_3(\theta_h)\mathbf{W}(\theta_h)\mathbf{D} \end{bmatrix}}_{\mathbf{G}} \underbrace{\begin{bmatrix} \mathbf{L}_\mathrm{P} \\ \mathbf{L}_\mathrm{S} \\ \mathbf{L}_\rho \end{bmatrix}}_{\mathbf{m}} \tag{7}$$

where $\mathbf{S}\in\mathbb{R}^{(mh)\times n}$ is the angle seismic gathers, including $h$ angles; $\mathbf{G}\in\mathbb{R}^{(mh)\times(3m+3)}$ is the multi-channel forward operator; $\mathbf{m}\in\mathbb{R}^{(3m+3)\times 1}$ is the 2D model parameter composed of the natural logarithm of P- and S-wave velocities, and density; $\mathbf{D}\in\mathbb{R}^{m\times(m+1)}$ is the first-order difference matrix shown in Eq. (4). Eq. (7) is the multi-channel forward model without rearranging the seismic traces, which can be simply expressed as:

$$\mathbf{S} = \mathbf{G}\mathbf{m} \tag{8}$$

Since $\mathbf{m}$ is a 2D matrix, it is difficult to directly implement complex constraints on $\mathbf{m}$. Rearranging the seismic traces to obtain a 1D $\overline{\mathbf{m}}$ vector can deal with this issue. In the $n$-trace case, the rearranged seismic data ($\overline{\mathbf{S}}\in\mathbb{R}^{(mnh)\times 1}$) can be expressed as:

$$\overline{\mathbf{S}} = \left[\overline{\mathbf{S}}_1^\mathrm{T}, \overline{\mathbf{S}}_2^\mathrm{T}, \ldots, \overline{\mathbf{S}}_h^\mathrm{T}\right]^\mathrm{T}, \overline{\mathbf{S}}_i = \left[(\overline{\mathbf{S}}_1(\theta_i))^\mathrm{T}, (\overline{\mathbf{S}}_2(\theta_i))^\mathrm{T}, \ldots, (\overline{\mathbf{S}}_n(\theta_i))^\mathrm{T}\right]^\mathrm{T} \tag{9}$$

where $\overline{\mathbf{S}}_i\in\mathbb{R}^{(mn)\times 1}(i=1,2,\ldots,h)$ is the rearranged angle gathers with the angle of $\theta_i$ and $\overline{\mathbf{S}}_j(\theta_i)(i=1,\ 2,\ \ldots,\ h,\ j=1,\ 2,\ \ldots,\ n)$ is the $j^{\mathrm{th}}$ trace of the angle gathers ($\overline{\mathbf{S}}(\theta_i)$). The rearranged 1D model parameters vector ($\overline{\mathbf{m}}\in\mathbb{R}^{(3(m+1)n)\times 1}$) is:

$$\overline{\mathbf{m}} = \left[\mathbf{L}_{\mathrm{P}1}^\mathrm{T}, \mathbf{L}_{\mathrm{P}2}^\mathrm{T}, \ldots, \mathbf{L}_{\mathrm{P}n}^\mathrm{T}, \mathbf{L}_{\mathrm{S}1}^\mathrm{T}, \mathbf{L}_{\mathrm{S}2}^\mathrm{T}, \ldots, \mathbf{L}_{\mathrm{S}n}^\mathrm{T}, \mathbf{L}_{\rho 1}^\mathrm{T}, \mathbf{L}_{\rho 2}^\mathrm{T}, \ldots, \mathbf{L}_{\rho \mathrm{n}}^\mathrm{T}\right]^\mathrm{T} \tag{10}$$

where $\mathbf{L}_{\mathrm{P}j}^\mathrm{T}$, $\mathbf{L}_{\mathrm{S}j}^\mathrm{T}$, and $\mathbf{L}_{\rho j}^\mathrm{T}(j=1,2,\ldots,n)$ are the vectors representing the nature logarithm of P-, S-velocity, and density at the $j^{\mathrm{th}}$ trace. The forward operator is:

$$\overline{\mathbf{G}} = \begin{bmatrix} \mathbf{C}_1^1\overline{\mathbf{W}}_1\overline{\mathbf{D}} & \mathbf{C}_1^2\overline{\mathbf{W}}_1\overline{\mathbf{D}} & \mathbf{C}_1^3\overline{\mathbf{W}}_1\overline{\mathbf{D}} \\ \mathbf{C}_2^1\overline{\mathbf{W}}_2\overline{\mathbf{D}} & \mathbf{C}_2^2\overline{\mathbf{W}}_2\overline{\mathbf{D}} & \mathbf{C}_2^3\overline{\mathbf{W}}_2\overline{\mathbf{D}} \\ \vdots & \vdots & \vdots \\ \mathbf{C}_h^1\overline{\mathbf{W}}_h\overline{\mathbf{D}} & \mathbf{C}_h^2\overline{\mathbf{W}}_h\overline{\mathbf{D}} & \mathbf{C}_h^3\overline{\mathbf{W}}_h\overline{\mathbf{D}} \end{bmatrix} \tag{11}$$

where $\overline{\mathbf{W}}_i\in\mathbb{R}^{(mn)\times(mn)} = kron(\mathbf{I}_n,\ \mathbf{W}(\theta_i))$, $\overline{\mathbf{D}}\in\mathbb{R}^{(mn)\times(mn+n)} = kron(\mathbf{I}_n, \mathbf{D})$, the operator $kron$ represents the Kronecker product, which can operate on two matrices of arbitrary size resulting in a block matrix and is a special form of tensor product (Loan, 2000; Yu et al., 2020). $\mathbf{I}_n$ is an $n$-order identity matrix. The coefficient matrices $\mathbf{C}_i^1$, $\mathbf{C}_i^2$, and $\mathbf{C}_i^3(i=1,2,\ldots,h)$ are:

$$\mathbf{C}_i^1 = \begin{bmatrix} c_1(\theta_i) & 0 & \cdots & 0 \\ 0 & c_1(\theta_i) & \cdots & 0 \\ \vdots & \vdots & \ddots & \vdots \\ 0 & 0 & \cdots & c_1(\theta_i) \end{bmatrix}_{mn\times mn}$$

$$\mathbf{C}_i^2 = \begin{bmatrix} c_2(\theta_i) & 0 & \cdots & 0 \\ 0 & c_2(\theta_i) & \cdots & 0 \\ \vdots & \vdots & \ddots & \vdots \\ 0 & 0 & \cdots & c_2(\theta_i) \end{bmatrix}_{mn\times mn}$$

$$\mathbf{C}_i^3 = \begin{bmatrix} c_3(\theta_i) & 0 & \cdots & 0 \\ 0 & c_3(\theta_i) & \cdots & 0 \\ \vdots & \vdots & \ddots & \vdots \\ 0 & 0 & \cdots & c_3(\theta_i) \end{bmatrix}_{mn\times mn} \tag{12}$$

Combine Eqs. (10)–(12), the rearranged multi-channel forward model can be simplified as follows (Yuan et al., 2015; Ma et al., 2018; Zhang et al., 2019):

$$\overline{\mathbf{S}} = \overline{\mathbf{G}}\overline{\mathbf{m}} \tag{13}$$

It is worth noting that the forward operator $\overline{\mathbf{G}}\in\mathbb{R}^{(mnh)\times(3mn+3n)}$ is a large-scale matrix, which will consume a lot of computer memory in pre-stack inversion. Moreover, several matrices of the same size as $\overline{\mathbf{G}}$ are required to achieve the conventional multi-channel inversion. The inversion efficiency is brutal to guarantee even if some optimization algorithms are adopted.

## 3. Reflection features constrained inversion

Seismic reflection features have been widely studied in the fields of multi-channel deconvolution, multi-channel seismic attenuation compensation, and multi-channel inversion, especially in complex geology. The application of refection features is mainly divided into two steps. One is to obtain seismic reflection features from the post-stack seismic profiles. The other is to construct a linear equation that can describe the relationship of model parameters between different seismic traces. This section introduces the conventional reflection features constrained inversion process, which mainly includes extracting reflection features, constructing a data-driven reflective features constraint term, and solving the objective functional by the BCD algorithm.

We obtain the reflection features by searching for the local shortest Euclidean distance between adjacent (Wang et al., 2021) (Fig. 1a). Euclidean distance can reflect the similarity of two random variables, and a short Euclidean distance indicates a high similarity of variables. We represent the reflection features with a matrix $\mathbf{K}$ that records the deviation $\kappa$. A negative $\kappa$ indicates the structural trends upward, and a positive $\kappa$ indicates the structural trends downward. Estimating the matrix $\mathbf{K}$ from the migrated seismic data can be expressed as follows:

$$\mathbf{K}(i,j) \approx \min_{\kappa} \sum_{\tau=-\omega}^{\omega} \|\mathbf{S}(i-\tau,j) - \mathbf{S}(i-\tau+\kappa,j')\|_2 \tag{14}$$

where $\mathbf{S}(i,j)$ represents the migrated seismic data located in the $i^{\text{th}}$ sampling point at the $j^{\text{th}}$ trace. $j'$ is the adjacent trace of $j$. $\tau$ is the index for calculating the local Euclidean distance within the time window $2\omega+1$. Since the structure usually bends gently locally, we search for the shortest Euclidean distance within $\kappa \in [-2\ \ 2]$. Based on the matrix $\mathbf{K}$, the relationship of the reflectivity between adjacent traces can be expressed:

$$\mathbf{r}(i,j) - \mathbf{r}(i+\mathbf{K}(i,j),j') = \varepsilon \tag{15}$$

where $\mathbf{r}(i,j)$ is the reflectivity of the $i^{\text{th}}$ sampling point at the $j^{\text{th}}$ trace, $\varepsilon$ is the minor error between the two reflectivities. We directly use the reflection features to express the relationship of the model parameters ($\mathbf{L}_{\text{P}}, \mathbf{L}_{\text{S}}, \mathbf{L}_{\rho} \in \mathbb{R}^{(m+1)\times n}$) between adjacent traces as follows:

$$\mathbf{L}_{\text{P}}(i,j) - \mathbf{L}_{\text{P}}(i+\mathbf{K}(i,j),j') = \varepsilon_{\text{P}}$$

$$\mathbf{L}_{\text{S}}(i,j) - \mathbf{L}_{\text{S}}(i+\mathbf{K}(i,j),j') = \varepsilon_{\text{S}}$$

$$\mathbf{L}_{\rho}(i,j) - \mathbf{L}_{\rho}(i+\mathbf{K}(i,j),j') = \varepsilon_{\rho} \tag{16}$$

We construct an operator to linearly represent the above relationship:

$$\mathbf{H}\bar{\mathbf{L}}_{\text{P}} = \boldsymbol{\varepsilon}_{\text{P}}, \mathbf{H}\bar{\mathbf{L}}_{\text{S}} = \boldsymbol{\varepsilon}_{\text{S}}, \mathbf{H}\bar{\mathbf{L}}_{\rho} = \boldsymbol{\varepsilon}_{\rho} \tag{17}$$

where $\bar{\mathbf{L}}_{\text{P}} = [\mathbf{L}_{\text{P1}}^{\text{T}}, \mathbf{L}_{\text{P2}}^{\text{T}}, \ldots, \mathbf{L}_{\text{Pn}}^{\text{T}}]^{\text{T}}$, $\bar{\mathbf{L}}_{\text{S}} = [\mathbf{L}_{\text{S1}}^{\text{T}}, \mathbf{L}_{\text{S2}}^{\text{T}}, \ldots, \mathbf{L}_{\text{Sn}}^{\text{T}}]^{\text{T}}$, $\bar{\mathbf{L}}_{\rho} = [\mathbf{L}_{\rho 1}^{\text{T}}, \mathbf{L}_{\rho 2}^{\text{T}}, \ldots, \mathbf{L}_{\rho \text{n}}^{\text{T}}]^{\text{T}}$ are the vectors that represent the rearranged parameters, and $\mathbf{L}_{\text{Pj}}^{\text{T}}$, $\mathbf{L}_{\text{Sj}}^{\text{T}}$, and $\mathbf{L}_{\rho j}^{\text{T}}$ ($j = 1, \ldots, n$) are the $j$th trace of 2D model parameters. The matrix $\mathbf{H} \in \mathbb{R}^{(mn)\times(mn+n)}$ can be expressed as:

$$\begin{cases} \mathbf{H}(m\times(j-1)+i, m\times(j-1)+i) = -1 \\ \mathbf{H}(m\times(j-1)+i, m\times j+i+\mathbf{K}(i,j)) = 1 \end{cases} \tag{18}$$

Next, we briefly explain the operator $\mathbf{H}$ to make it easier to understand. If $\mathbf{H}$ is used to constrain $\bar{\mathbf{L}}_{\text{P}}$, meaning that $[\mathbf{H}\bar{\mathbf{L}}_{\text{P}}]_{\chi} = [\bar{\mathbf{L}}_{\text{P}}]_{\chi+m+\mathbf{K}(i,j)} - [\bar{\mathbf{L}}_{\text{P}}]_{\chi}$, where $[]_{\chi}$ represents the $\chi^{\text{th}}$ element of the vector and $\chi = m\times(j-1)+i$. Therefore, the reflective features constraint term for three parameters inversion can be expressed as follows:

$$\min_{\bar{\mathbf{m}}} \|\bar{\mathbf{H}}\bar{\mathbf{m}}\|_2^2 \tag{19}$$

where $\bar{\mathbf{H}} \in \mathbb{R}^{(3mn)\times(3mn+3n)} = kron(\mathbf{I}_3, \mathbf{H})$, $\mathbf{I}_3$ is a 3-order identity matrix. Based on the multi-channel forward model (Eq. (13)), The objective function of conventional reflection features constrained inversion can be given as follows:

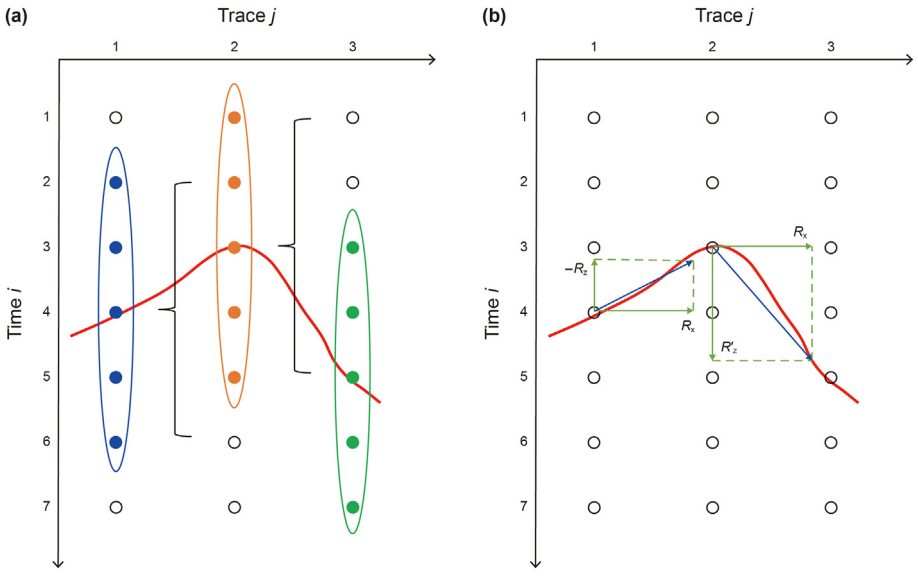


**Fig. 1.** An example of (a) estimating and (b) characterizing the seismic reflection features. The red line represents the seismic reflection event. For the former, the ellipse denotes the time windows, and the black brackets denote the neighborhood where the shortest local Euclidean distance is searched. According to the reflection event, there are $\mathbf{K}(4,1) = -1$ and $\mathbf{K}(3,2) = 2$. In the proposed characterization of reflection features, the trend of reflection events is decomposed into lateral and vertical differences, as indicated by the green arrows.

$$f(\overline{\mathbf{m}}) = \min_{\overline{\mathbf{m}}} \|\overline{\mathbf{S}} - \overline{\mathbf{G}}\overline{\mathbf{m}}\|_2^2 + \nu\|\overline{\mathbf{H}}\overline{\mathbf{m}}\|_2^2 \tag{20}$$

where $\nu > 0$ is the regularization parameter that controls the weight of the reflection features constraint. Noting that matrices $\overline{\mathbf{G}}$ and $\overline{\mathbf{H}}$ are large-scale matrices that are difficult to inverse and have high computational costs. We adopt the BCD algorithm to deal with this issue. This algorithm is required to minimize Eq. (20) trace-by-trace in each iteration. In the $k^{\text{th}}$ iteration, a particular trace is minimized by:

$$\overline{\mathbf{m}}_j^{k+1} = \text{argmin} f\left(\overline{\mathbf{m}}_1^k, \cdots, \overline{\mathbf{m}}_{j-1}^k, \overline{\mathbf{m}}_j^k, \overline{\mathbf{m}}_{j+1}^{k-1}, \cdots, \overline{\mathbf{m}}_n^{k-1}\right) \tag{21}$$

where $\overline{\mathbf{m}}_j^k (j = 1, \ldots, n)$ represents the $j^{\text{th}}$ trace of the model parameters; $f$ is the objective function of reflection features constrained inversion. The detailed process can refer to *Algorithm 1*.

**Algorithm 1.** *Reflection features constrained inversion with BCD algorithm*

1) **Initialize**: set $\overline{\mathbf{m}} = \overline{\mathbf{m}}_{\text{low}}$. $\overline{\mathbf{m}}_{\text{low}}$ is the rearranged low-wavenumber model obtained by interpolation extrapolation and smoothing along the horizon with the log curves, including P-, S-velocity, and density.
2) Obtain the reflection features using Eq. (14). Then, construct the operator $\overline{\mathbf{H}}$.
3) **While** $\|\overline{\mathbf{m}}^{k+1} - \overline{\mathbf{m}}^k\|^2 > \varepsilon$ **do**
4) **for** $i = 1, \ldots, n$.
5) $\overline{\mathbf{m}}_j^{k+1} = \text{argmin} f(\overline{\mathbf{m}}_1^k, \cdots, \overline{\mathbf{m}}_{j-1}^k, \overline{\mathbf{m}}_j^k, \overline{\mathbf{m}}_{j+1}^{k-1}, \cdots, \overline{\mathbf{m}}_n^{k-1})$
6) **end**
7) **end**
8) $[\mathbf{V}_{\text{P}} \quad \mathbf{V}_{\text{S}} \quad \boldsymbol{\rho}]^{\text{T}} = \exp(\overline{\mathbf{m}})$

## 4. Fast reflection features constrained inversion (FRCI)

The BCD algorithm makes it possible for conventional reflection features constrained inversion to invert more seismic traces simultaneously, but at the expense of efficiency due to multiple iterations and traversals. To address this issue, we proposed a fast reflection features constrained inversion. By re-characterizing the seismic reflection features, a new way was developed to introduce the reflection features constraints without rearranging seismic traces. Different from the conventional seismic trace rearrangement, we adopt the Hadamard product operator to introduce seismic reflection features, avoiding the generation of large-scale operators such as $\overline{\mathbf{G}}$ and $\overline{\mathbf{H}}$. This section constructs the new reflection features regularization terms and derives a fast optimization algorithm for reflection features constrained multi-channel inversion.

### 4.1. Constructing the reflection features regularization terms

Unlike the conventional reflection features regularization terms consisting of large-scale operators, we construct the computationally well-behaved regularization terms without seismic trace rearrangement. We have characterized complex reflection features with matrices and constructed the constraint operators. As shown in Fig. 1b, the direction of the reflective features, represented by the blue arrow line, can be decomposed into lateral and vertical differences. Since $k$ is limited to $[-2 \quad 2]$, we can use the lateral and vertical first- and second-order partial derivatives to represent the trend of reflectivity at any point.

Based on the 2D multi-channel forward model (Eq. (8)), we directly give the reflection features regularization term along with the seismic reflection events:

$$f(\mathbf{m}) = \min_{\mathbf{m}} \left\|\mathbf{m}\mathbf{R}_x + \mathbf{H}_1 \circ (\mathbf{R}_z\mathbf{m}) + \mathbf{H}_2 \circ (\mathbf{R}_z'\mathbf{m})\right\|_{\text{F}}^2 \tag{22}$$

where $\|\|_{\text{F}}$ is the Frobenius norm specifically for the matrix, representing the square root of the sum of squares of all elements (Gholami, 2016; Yang et al., 2022), and it can be defined as $\|\mathbf{A}\|_{\text{F}} = \sqrt{\sum_i^m \sum_j^n a_{ij}^2}$, where $\mathbf{A} = [a_{ij}]_{m\times n}$. $\circ$ is the Hadamard product operator, representing the product of corresponding elements of two matrices of the same size. $\mathbf{R}_x = \mathbf{D}^{\text{T}}$ and $\mathbf{R}_z = \mathbf{D}$ are the first-order lateral and vertical differences, respectively. $\mathbf{R}_z'$ is a special vertical difference and can be expressed as:

$$\mathbf{R}_z' = \begin{bmatrix} -1 & 0 & 1 & 0 & \cdots & 0 \\ 0 & -1 & 0 & 1 & \cdots & 0 \\ \vdots & \vdots & \ddots & \ddots & \ddots & \vdots \\ 0 & 0 & \cdots & -1 & 0 & 1 \end{bmatrix} \tag{23}$$

The matrices $\mathbf{H}_1 = [\mathbf{K}_1^{\text{T}}, \mathbf{K}_1^{\text{T}}, \mathbf{K}_1^{\text{T}}]^{\text{T}}$ and $\mathbf{H}_2 = [\mathbf{K}_2^{\text{T}}, \mathbf{K}_2^{\text{T}}, \mathbf{K}_2^{\text{T}}]^{\text{T}}$, where

$$\mathbf{K}_1(i,j) = \begin{cases} 0 & abs(\mathbf{K}(i,j)) \neq 1 \\ sign(\mathbf{K}(i,j))\ abs(\mathbf{K}(i,j)) & = 1 \end{cases}$$

$$\mathbf{K}_2(i,j) = \begin{cases} 0 & abs(\mathbf{K}(i,j)) \neq 2 \\ sign(\mathbf{K}(i,j))\ abs(\mathbf{K}(i,j)) & = 2 \end{cases} \tag{24}$$

and the operator $sign(x) = \begin{cases} -1 & x < 0 \\ 0 & x = 0 \\ 1 & x > 0 \end{cases}$.

To ensure the stability and convergence of the multi-channel inversion, we further considered the constraints in the direction perpendicular to the reflection events, and the reflection features regularization terms can be expressed as follows:

$$\begin{aligned} f(\mathbf{m}) = \min_{\mathbf{m}} &\left\|\mathbf{m}\mathbf{R}_x + \mathbf{H}_1 \circ (\mathbf{R}_z\mathbf{m}) + \mathbf{H}_2 \circ (\mathbf{R}_z'\mathbf{m})\right\|_{\text{F}}^2 \\ &+ \left\|\mathbf{R}_z\mathbf{m} - \mathbf{H}_1 \circ (\mathbf{m}\mathbf{R}_x) - \mathbf{H}_2 \circ (\mathbf{m}\mathbf{R}_x')\right\|_{\text{F}}^2 \end{aligned} \tag{25}$$

where

$$\mathbf{R}_x' = \begin{bmatrix} -1 & 0 & \cdots & 0 \\ 0 & -1 & \cdots & 0 \\ 1 & 0 & \ddots & \vdots \\ 0 & 1 & \ddots & -1 \\ \vdots & \vdots & \ddots & 0 \\ 0 & 0 & \cdots & 1 \end{bmatrix} \tag{26}$$

and $\left\|\mathbf{R}_z\mathbf{m} - \mathbf{H}_1 \circ (\mathbf{m}\mathbf{R}_x) - \mathbf{H}_2 \circ (\mathbf{m}\mathbf{R}_x')\right\|_{\text{F}}^2$ is the regularization term perpendicular to the reflection events. It is worth noting that the reflection features regularization (Eq. (24)) can degenerate into TV regularization when the stratum is horizontally distributed. Therefore, the proposed method also inherits the high-efficiency property of TV regularization multi-channel inversion.

### 4.2. Pre-stack multi-channel inversion with the fast optimization scheme

Eq. (24) gives the regularization terms parallel and perpendicular to the reflection events via the particular symbol Hadamard product operator. Different from the conventional reflection features regularization term with the large-scale operator, the new terms can be represented with a few small-size matrices. Combine the penalty term, the objective function of the fast reflection features constrained inversion can be expressed as follows:

$$f(\mathbf{m}) = \min_{\mathbf{m}} \|\mathbf{S} - \mathbf{G}\mathbf{m}\|_F^2 + \lambda \left\|\mathbf{m}\mathbf{R}_x + \mathbf{H}_1 \circ (\mathbf{R}_z\mathbf{m}) + \mathbf{H}_2 \circ (\mathbf{R}_z'\mathbf{m})\right\|_F^2 + \alpha \left\|\mathbf{R}_z\mathbf{m} - \mathbf{H}_1 \circ (\mathbf{m}\mathbf{R}_x) - \mathbf{H}_2 \circ (\mathbf{m}\mathbf{R}_x')\right\|_F^2 \tag{27}$$

where $\lambda > 0$ and $\alpha > 0$ are the weights of the regularization terms parallel and perpendicular to the seismic reflection events. $\|\mathbf{S} - \mathbf{G}\mathbf{m}\|_F^2$ is a penalty term to control the data misfit. Due to the Frobenius norm and Hardmard product operator, the minimization problem is difficult to solve directly. We have derived a fast optimization scheme to deal with it based on the convex optimization method. First, Eq. (25) can be written as an unconstrained minimization problem:

$$\begin{aligned} &\min \|\mathbf{S}-\mathbf{G}\mathbf{m}\|_F^2+\lambda\left\|\mathbf{X}_1+\mathbf{H}_1 \circ \mathbf{X}_2+\mathbf{H}_2 \circ \mathbf{X}_2'\right\|_F^2+\alpha\left\|\mathbf{X}_2-\mathbf{H}_1 \circ \mathbf{X}_1-\mathbf{H}_2 \circ \mathbf{X}_1'\right\|_F^2 \\ &\text{s.t} \mathbf{m}\mathbf{R}_x=\mathbf{X}_1, \mathbf{m}\mathbf{R}_x'=\mathbf{X}_1', \mathbf{R}_z\mathbf{m}=\mathbf{X}_2, \mathbf{R}_z'\mathbf{m}=\mathbf{X}_2' \end{aligned} \tag{28}$$

where $\mathbf{X}_1$, $\mathbf{X}_1'$, $\mathbf{X}_2$, and $\mathbf{X}_2'$ are variables, representing the first- and second-order difference along with the horizontal and vertical directions, respectively. Based on the ADMM optimization that can inherit the advantage of dual decomposition and the convergence efficiency of the multiplier method (Boyd et al., 2010), the augmented Lagrangian form of Eq. (26) can be given as follows:

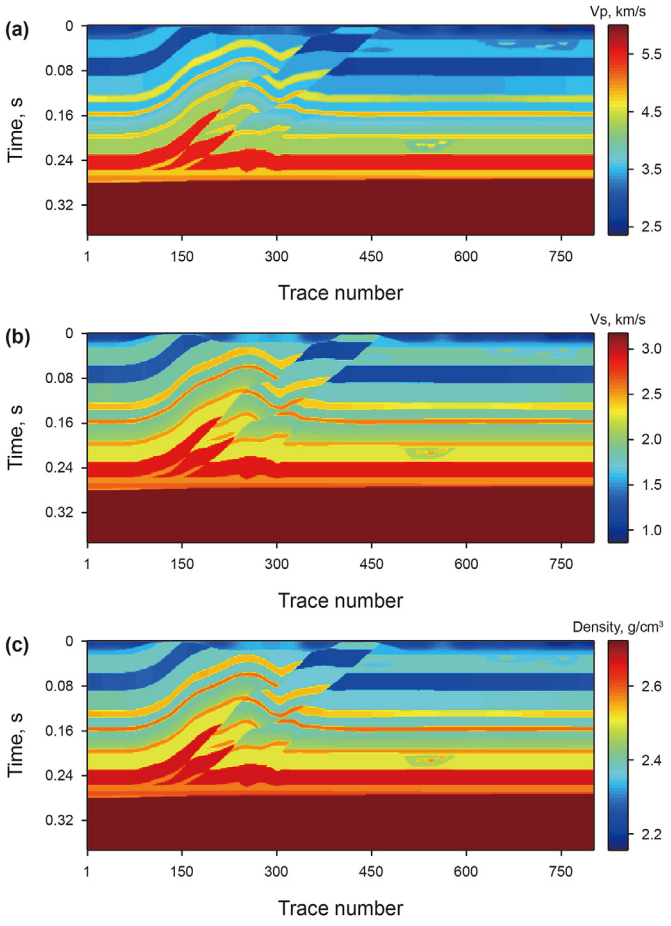


**Fig. 2.** The true models of (a) P-velocity, (b) S-velocity, and (c) density obtained from the 3D overthrust model. They include 801 traces and each trace with 187 sampling points.

$$\begin{aligned} L_\zeta = \min\Big\{ &\|\mathbf{S}-\mathbf{G}\mathbf{m}\|_F^2+\lambda\left\|\mathbf{X}_1+\mathbf{H}_1 \circ \mathbf{X}_2+\mathbf{H}_2 \circ \mathbf{X}_2'\right\|_F^2+\alpha\left\|\mathbf{X}_2-\mathbf{H}_1 \circ \mathbf{X}_1-\mathbf{H}_2 \circ \mathbf{X}_1'\right\|_F^2+(\zeta/2)\left(\|\mathbf{m}\mathbf{R}_x-\mathbf{X}_1+\mathbf{Z}_1/\zeta\|_F^2+\|\mathbf{m}\mathbf{R}_x'-\mathbf{X}_1'+\mathbf{Z}_1'/\zeta\|_F^2\right) \\ &+(\zeta/2)\left(\|\mathbf{R}_z\mathbf{m}-\mathbf{X}_2+\mathbf{Z}_2/\zeta\|_F^2+\|\mathbf{R}_z'\mathbf{m}-\mathbf{X}_2'+\mathbf{Z}_2'/\zeta\|_F^2\right)\Big\} \end{aligned} \tag{29}$$

where $\mathbf{Z}_1$, $\mathbf{Z}_1'$, $\mathbf{Z}_2$, and $\mathbf{Z}_2'$ are the Lagrange multipliers or dual variables. $\zeta > 0$ is an augmented Lagrangian parameter indicating the iteration step size. The optimization of Eq. (27) requires 9 steps in each iteration, including $\mathbf{m}$-, $\mathbf{X}_1$-, $\mathbf{X}_1'$-, $\mathbf{X}_2$-, $\mathbf{X}_2'$-, $\mathbf{Z}_1$-, $\mathbf{Z}_1'$-, $\mathbf{Z}_2$-, and $\mathbf{Z}_2'$-minimization. It is worth noting that the update of $\mathbf{m}$ is to solve a well-known Sylvester equation with the form $\mathbf{A}\mathbf{m} + \mathbf{m}\mathbf{B} = \mathbf{C}$, which can be solved by the eigen decomposition strategy (Gholami, 2016). Algorithm 2 is the pseudocode of the fast reflection features constrained inversion, and the details for the derivation can be found in Appendix A.

**Algorithm 2.** *Fast reflection features constrained inversion*

1) **Inputs:** set $\mathbf{m} = \mathbf{m}_{\text{low}}$, where $\mathbf{m}_{\text{low}}$ is the initial model. Then, set $\mathbf{X}_1 = \mathbf{m}\mathbf{R}_x$, $\mathbf{X}_1' = \mathbf{m}\mathbf{R}_x'$, $\mathbf{X}_2 = \mathbf{R}_z\mathbf{m}$, $\mathbf{X}_2' = \mathbf{R}_z'\mathbf{m}$, $\mathbf{Z}_1 = 0$, $\mathbf{Z}_1' = 0$, $\mathbf{Z}_2 = 0$, and, $\mathbf{Z}_2' = \mathbf{0}$. Set $\lambda$, $\alpha$, the iterative step size $\zeta$, and the convergence threshold $\varepsilon$.
2) Obtain the reflection features using Eq. (14). Then, construct the operator $\mathbf{H}_1$ and $\mathbf{H}_2$ through Eq. (24).
3) If the termination condition $\|\mathbf{m}^{k+1} - \mathbf{m}^k\|^2 < \varepsilon$ is not satisfied, **execute the loop**:
4) **step1:** update the model parameter $\mathbf{m}^{k+1}$ using the Sylvester equation (Eq. (A-4)), which can be solved though eigenvalue decomposition.
5) **step2:** update the variables $\mathbf{X}_1$, $\mathbf{X}_2$, $\mathbf{X}_1'$, and $\mathbf{X}_2'$ by minimizing the 2nd to 5th sub-equations in Eq. (A-1). See Eqs. (A-12) and (A-13) for the solution.
6) **step3:** update the dual variables $\mathbf{Z}_1$, $\mathbf{Z}_2$, $\mathbf{Z}_1'$, and $\mathbf{Z}_2'$ using the Eq. (A-14).
7) **end**
8) **Outputs:** obtain the model parameters by $[\mathbf{V}_P \quad \mathbf{V}_S \quad \boldsymbol{\rho}]^T = \exp(\mathbf{m})$

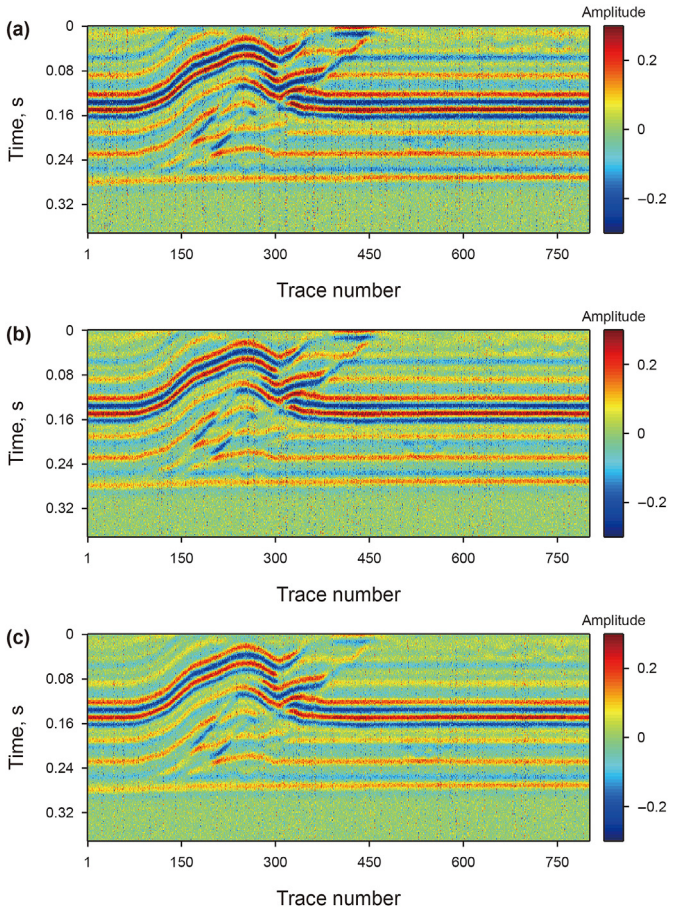


**Fig. 3.** The noisy seismic gathers with angles of (a) 10°, (b) 20°, (c) 30°, which obtained by the true models and a 30Hz Ricker wavelet based on the Aki-Richard equation. The synthetic gathers have been disturbed by 10% Gaussian noise, and 30% seismic traces are randomly selected to add Gaussian noise with an SNR = 1.

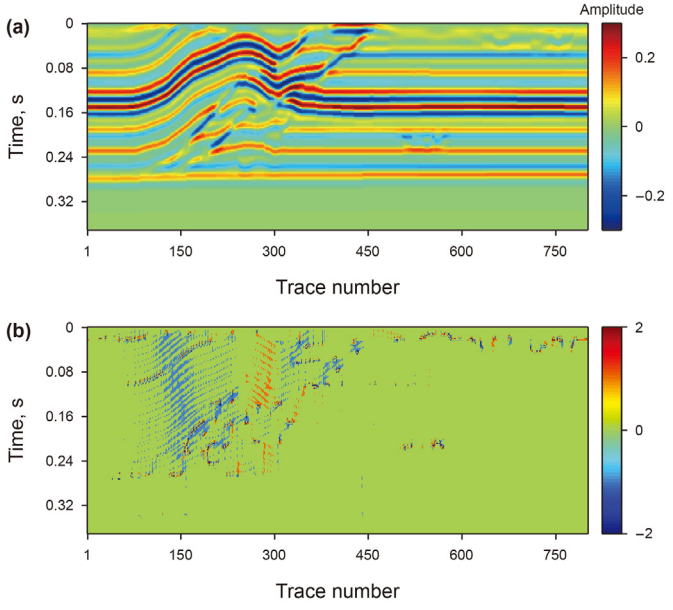


**Fig. 4.** (a) The synthesized post-stack seismic data. (b) The reflection features estimated from the post-stack profile.

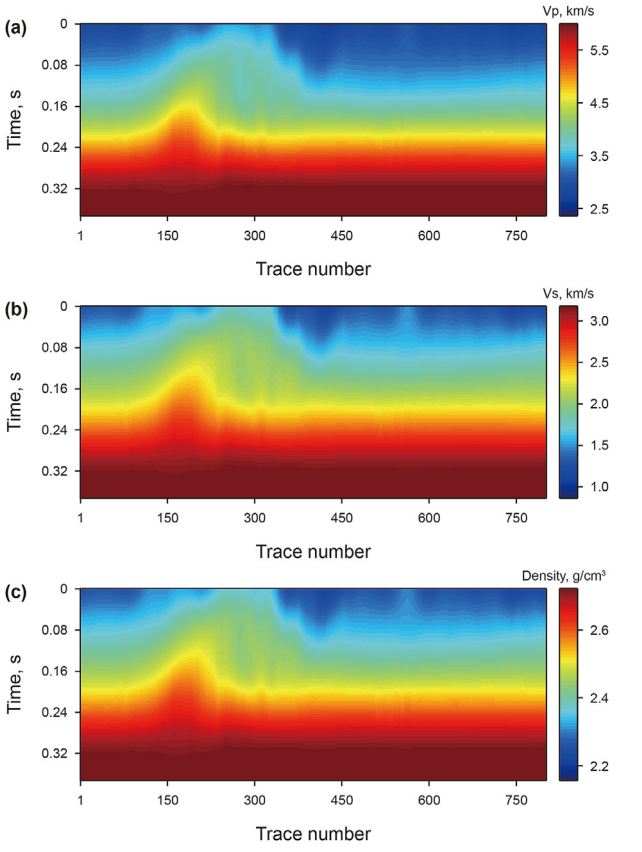


**Fig. 5.** The low-wavenumber model of (a) P-velocity, (b) S-velocity, and (c) density obtained by low-pass filtering at 5Hz on the true models.

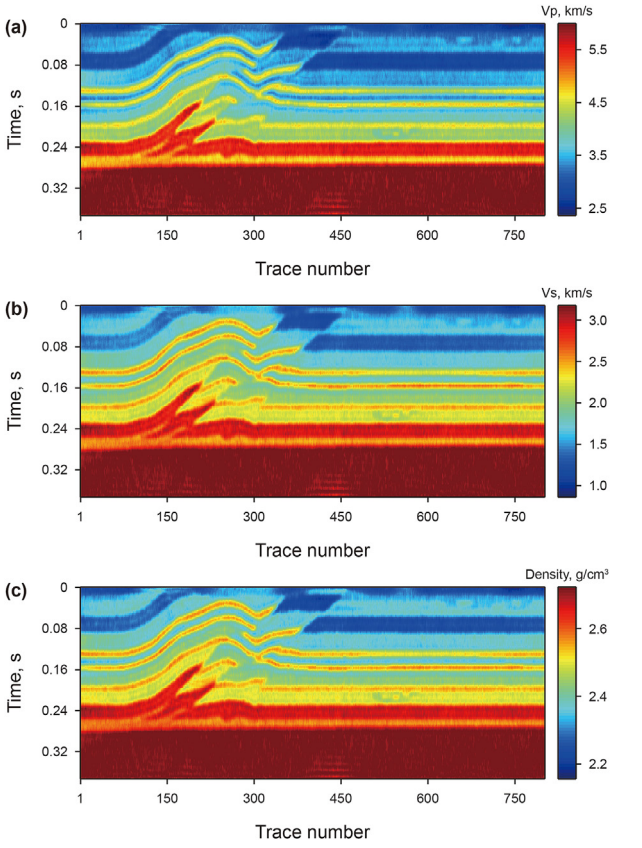


**Fig. 6.** The estimated (a) P-velocity, (b) S-velocity, and (c) density by the conventional reflection features constrained inversion.

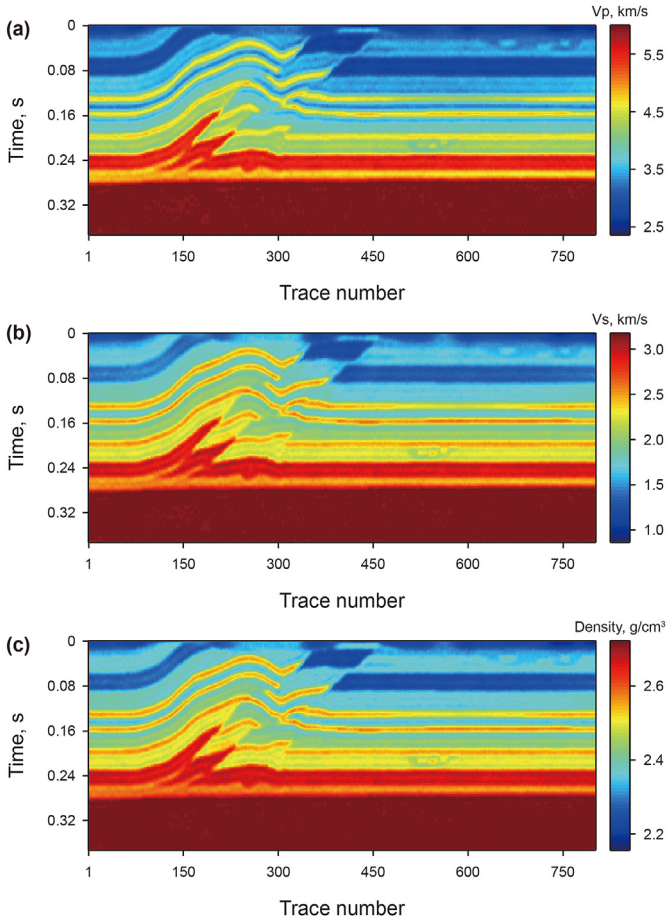


**Fig. 7.** The estimated (a) P-velocity, (b) S-velocity, and (c) density by the proposed FRCI. Compared with conventional inversion, the inversion results are of higher quality and closer to the true model.

## 5. Simulation experiment

The feasibility and effectiveness of the proposed FRCI algorithm have been tested on the Overthrust model. Fig. 2 shows the true P-velocity, S-velocity, and density model, which include 801 traces and 187 sampling points per trace. The angle gathers with angles of 10°, 20°, and 30° (Fig. 3) are synthesized by Eq. (7) using the 30Hz Ricker wavelet. 10% Gaussian noise was added to the synthetic gathers to evaluate the uncertainty of the inversion results. To further examine the noise resistance of the proposed algorithm, randomly select 30% of seismic traces to add noise of SNR = 1.

Estimating seismic reflection features is a critical step in reflection features constrained inversion. Therefore, we adopted Yu's strategy (Yu et al., 2020) to obtain the reflection features from the post-stack seismic data through Eq. (14), as shown in Fig. 4. Fig. 5 shows the initial P-velocity, S-velocity, and density obtained by 5Hz low-pass filtering on the true models.

The efficiency and reliability of the FRCI algorithm were compared with the conventional reflection features constrained inversion method. In this work, we treat the direct estimation of model parameters by Algorithm 1 from seismic data as a conventional inversion method. Fig. 6 shows the estimated P-velocity, S-

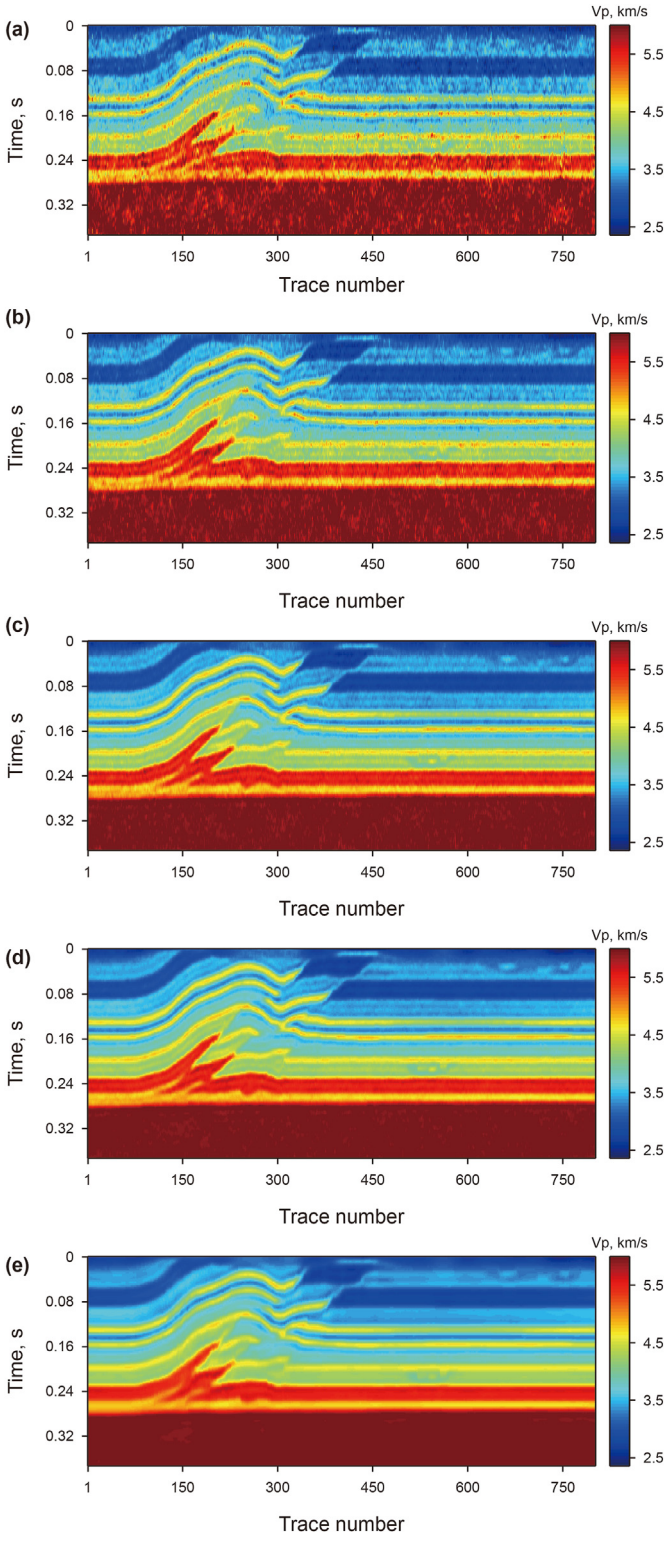


**Fig. 8.** The estimated P-velocity when the weight of regularization term parallel to the reflection features $\lambda$ is (a) 0.0001, (b) 0.001, (c) 0.01, (d) 0.1, (e) 1. The model is discontinuous when $\lambda$ is 0.0001 and 0.001, especially $\lambda = 0.0001$. Conversely, iterations with large weight $\lambda = 1$ produce a too smooth model. The most satisfactory model can be obtained when $\lambda = 0.1$.

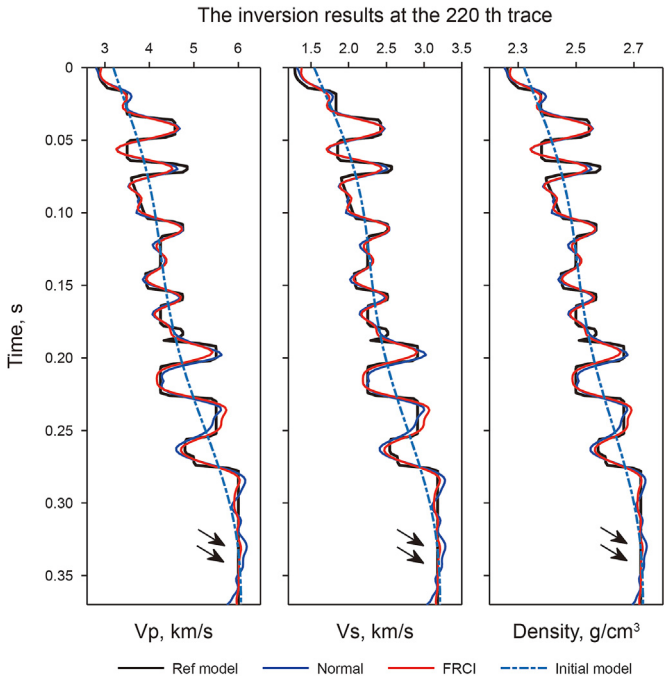


**Fig. 9.** Comparison of inversion results with the true model at 220th trace. The light blue dashed line is the low-wavenumber model, and the black line represents the true model. The blue and red lines are estimated results by conventional reflection features constrained inversion and FRCI algorithm, respectively. The red lines are closer to the reference model.

velocity, and density by the conventional method. In general, the inversion results follow the true model indicating that our inversion work is reliable. However, the continuity still needs improvement, and some areas seem challenging to converge, especially a high-speed layer at the bottom. Fig. 7 shows the estimated P-velocity, S-velocity, and density by the proposed FRCI algorithm. Compared with the conventional method, the inversion results of our approach are closer to the true model and perform better in continuity.

The weight of the regularization term parallel to the reflection features $\lambda$ is an important factor affecting the continuity of the inversion results. We compared the inversion results with different $\lambda$ to evaluate the uncertainty of the inversion. Fig. 8a–e shows the estimated P-velocities when $\lambda$ is 0.0001, 0.001, 0.01, 0.1, and 1. The larger $\lambda$ is chosen, the more continuous the inversion results are. However, a too large $\lambda$ will produce a too smooth model. We can obtain a relatively satisfactory result for this seismic data set when $\lambda$ is 0.1. Actually, the value of $\lambda$ is related to the noise level of seismic data. In addition, $\lambda$ can be appropriately increased to suppress the noise when the SNR of seismic data is low.

The accuracy of the inversion results was checked at trace number = 220 by the single trace comparison, as shown in Fig. 9. The black lines and light blue dashed lines represent the true and initial models, respectively. The blue and red lines represent the inversion results of the conventional method and the proposed FRCI algorithm. It can be seen that the blue and red lines are in good agreement with the black lines, which ensures the credibility of the inversion. However, the red line is closer to the black line, especially where the black arrows point, which may be caused by noise, making it difficult for conventional methods to converge. Fig. 10a shows the relative errors of the estimated P-velocity, S-velocity, and density with different $\lambda$ by the proposed FRCI algorithm. P-velocity has the highest accuracy, and its error is smaller than the S-velocity and density. It is worth noting that the P-velocity, S-velocity, and density with minor errors can be simultaneously obtained when $\lambda$ is 0.1. Furthermore, the convergence time and errors statistics show that our method performs better in efficiency and reliability than the conventional method, as shown in Fig. 10b. Compared with the conventional method, the proposed method dramatically improves the inversion efficiency while ensuring accuracy.

## 6. Field data example

Another dataset from an oilfield was selected to test the effectiveness of the proposed approach. This area is located in a slope zone, and the development of faults and coal seams exacerbates the uncertainty of pre-stack seismic inversion. Similarly, we compared

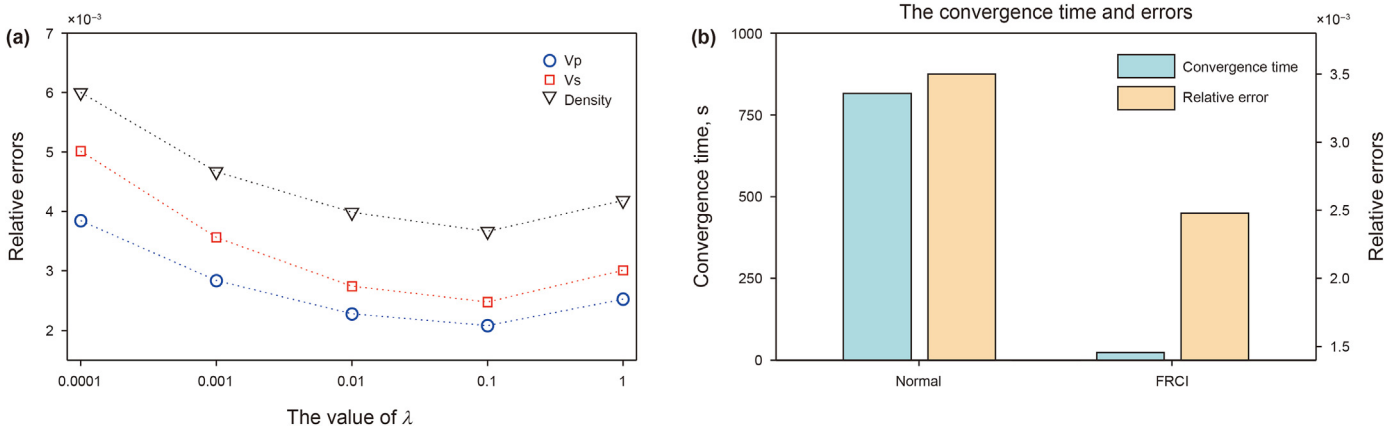


**Fig. 10.** (a) The relative errors between the true models and estimated P-, S-velocity, density when $\lambda$ is 0.0001, 0.001, 0.01, 0.1, and 1. The relative errors are calculated by $\|\overline{\mathbf{m}} - \mathbf{m}\|_F^2 / \|\mathbf{m}\|_F^2$, where $\overline{\mathbf{m}}$ is the inversion results; $\mathbf{m}$ is the true models. The inversion results of P- and S-velocity, and density closest to the true models can be obtained simultaneously when $\lambda = 0.1$. (b) The comparison of convergence time and error between conventional reflection features constrained inversion and the proposed FRCI. The proposed FRCI performs better in efficiency and accuracy, especially the inversion efficiency.

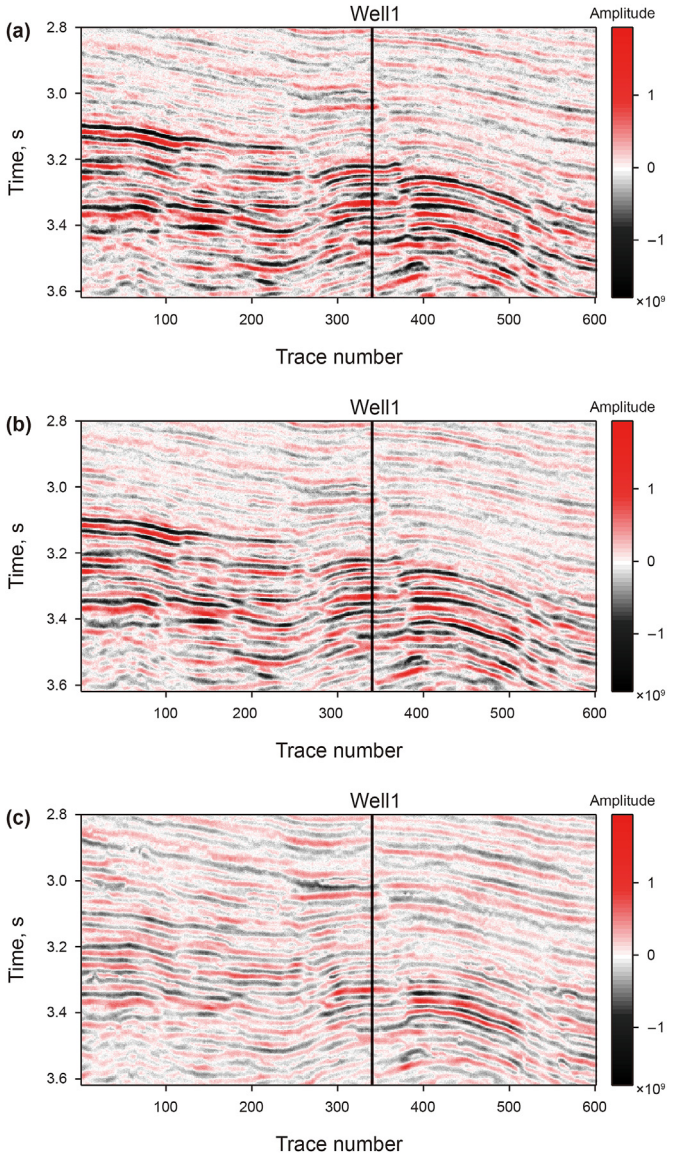


**Fig. 11.** The field seismic gathers with angles of (a) 6°, (b) 18°, (c) 30°. The black line indicates the location of Well1.

the conventional reflection features constrained inversion and proposed the FRCI algorithm. Fig. 11 shows the field seismic profile with angles of 6°, 18°, and 30° obtained from the CRP gathers by some necessary processing such as filtering, multiple correction, static correction, transform to angle gathers, and partial angle stacking. The black line indicates the location of Well1, which is used as a reference model. The seismic frequency mainly varies from 9 Hz to 60 Hz, and the sampling interval is 2 ms.

Expanding the neighborhood range $k$ when estimating the reflection features will complicate the objective function. In this work, we compared the inversion results with different $k$. Fig. 12 shows the estimated reflection features when neighborhood range $k$ is $[-2\ 2]$ and $[-3\ 3]$, respectively. The two profiles differ little, even though different color bars are adopted. The phenomenon is reasonable because the stratum hardly bends sharply locally.

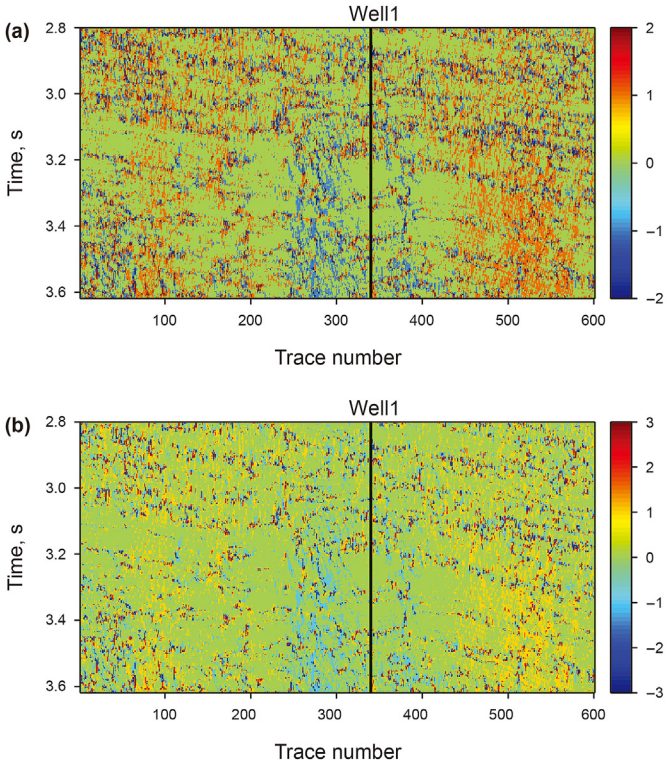


**Fig. 12.** The estimated reflection features when neighborhood range $\kappa$ is (a) [-2 2] and (b) [-3 3]. This work explores whether it is necessary to widen the neighborhood since the complexity of the objective function will be exaggerated when $\kappa$ is extended.

The conventional reflection features constrained inversion based on the BCD algorithm are also used as a reference to test the performance of the FRCI algorithm. Fig. 13 shows the estimated P-velocity, S-velocity, and density by the conventional method when the parameter $k$ is set to $[-2\ 2]$. The black lines at Well1 represent the corresponding curves, respectively. They are obtained by high-cut filtering the logging curves to the seismic frequency band. The inversion results of the proposed FRCI algorithm are generally close to the estimated results by the conventional method (Fig. 14), but perform better in some local areas, especially within the black ellipse. Compared with the conventional method, the estimated P-velocity by the proposed FRCI has better layering and continuity within the ellipse. Fig. 15 shows the inversion results estimated by the FRCI when the parameter $k$ is $[-3\ 3]$. It can be seen that when $k$ is $[-2\ 2]$ and $[-3\ 3]$, the difference in the inversion results is slight. Even the performance of the FRCI drops in some areas after expanding the neighborhood range $k$, which may be caused by the complex objective function reducing the accuracy of the solution. Therefore, expanding $k$ will complicate the objective function and usually has no apparent benefit to the accuracy of inversion results, consistent with Yu's conclusion (Yu et al., 2020).

We compared the inversion results estimated by the conventional method and FRCI algorithm with the reference model at Well1, as shown in Fig. 16. The brown and green lines represent the reference and initial models, respectively. The reference model is obtained by filtering the logging curves to the seismic frequency band. The initial model is obtained by extrapolation and smoothing the curves of Well1 along with the layers. The blue and red lines are inversion results estimated by the conventional and proposed FRCI

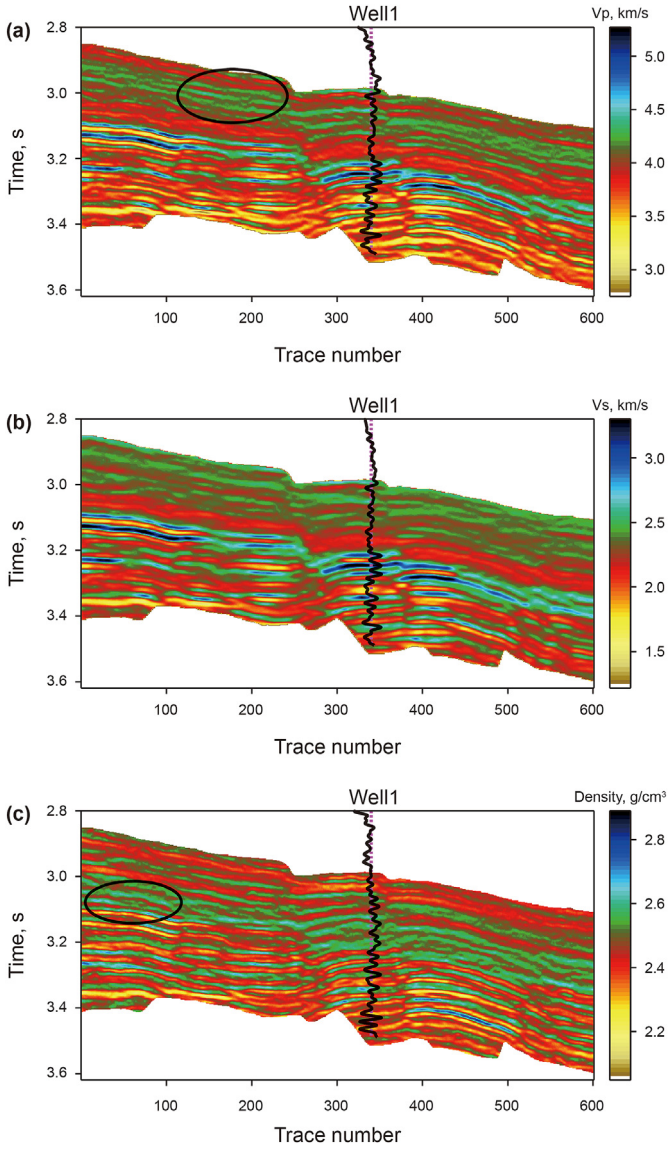


**Fig. 13.** The estimated (a) P-velocity, (b) S-velocity, and (c) density by conventional reflection features constrained inversion when $\kappa \in [-2\ 2]$.

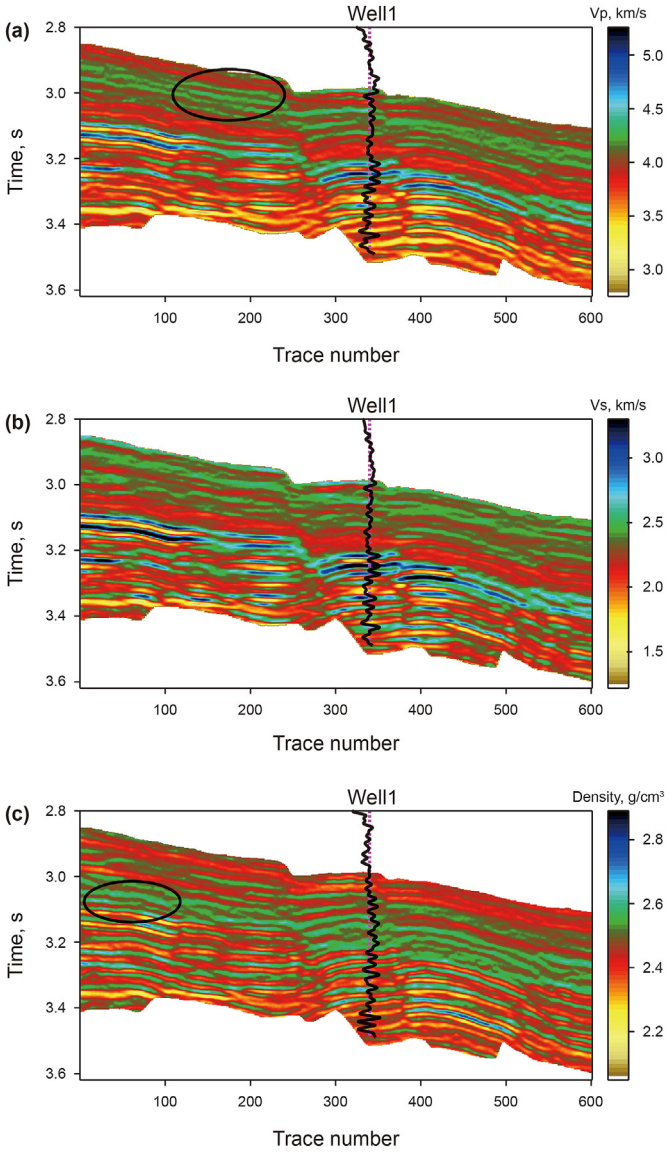


**Fig. 14.** The estimated (a) P-velocity, (b) S-velocity, and (c) density by the proposed FRCI method when $\kappa \in [-2\ 2]$. Compared with the inversion results obtained by conventional method, the FSCI performs better in continuity, especially in the ellipse area.

methods. The inversion relative errors and convergence efficiency is shown in Fig. 17, as in the simulation experiments. The proposed algorithm has smaller errors in Well1 and are extremely efficient, which proves the effectiveness of FRCI algorithm.

## 7. Discussion

The stability and continuity of the seismic pre-stack inversion are issues that deserve attention. The reflection features constrained inversion can efficiently deal with them. Such conventional methods have to handle the large-scale matrices due to the rearrangement of seismic traces, limiting their wide application in the pre-stack seismic inversion. We propose an FRCI algorithm to improve the inversion efficiency while ensuring accuracy. We test the feasibility and effectiveness of the proposed algorithm on two data sets, the Overthrust model (Fig. 3) and a field work area with fault development (Fig. 11). We estimate the seismic reflection features from the Overthrust model and field seismic data with different neighborhood ranges $\kappa$. The inversion results (Figs. 6–7 and Figs. 13 and 14) and relative errors (Figs. 10 and 17a) show that our algorithm performs better in continuity and accuracy than the conventional reflection features constrained inversion. The comparisons of convergence efficiency indicate that the FRCI algorithm performs extremely well in computation.

When estimating the seismic reflection features using the shortest Euclidean distance, two important parameters need to be concerned, the time windows $w$ and neighborhood ranges $\kappa$. A smaller time window can obtain more accurate seismic reflection features when the SNR of seismic data is high, but the noise resistance capability is worse. Different from the studies in which

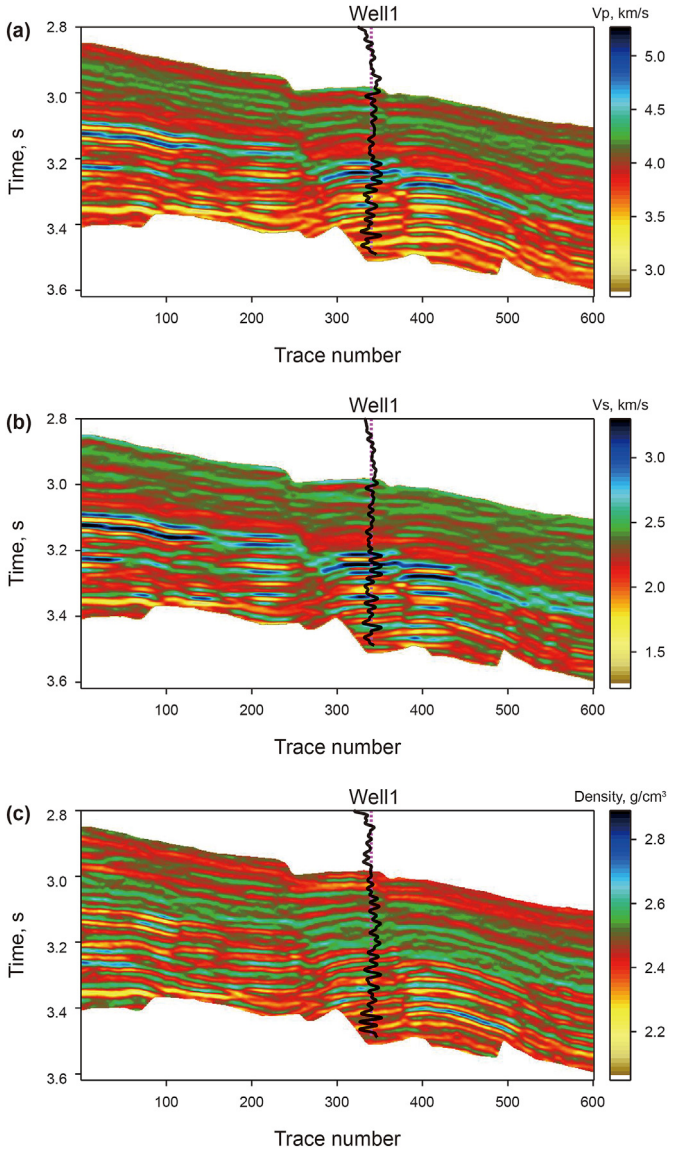


**Fig. 15.** The estimated (a) P-velocity, (b) S-velocity, and (c) density by the proposed FRCI method when $\kappa \in [-\ 3\ 3]$. They are similar to the inversion results when $\kappa \in [-\ 2\ 2]$.

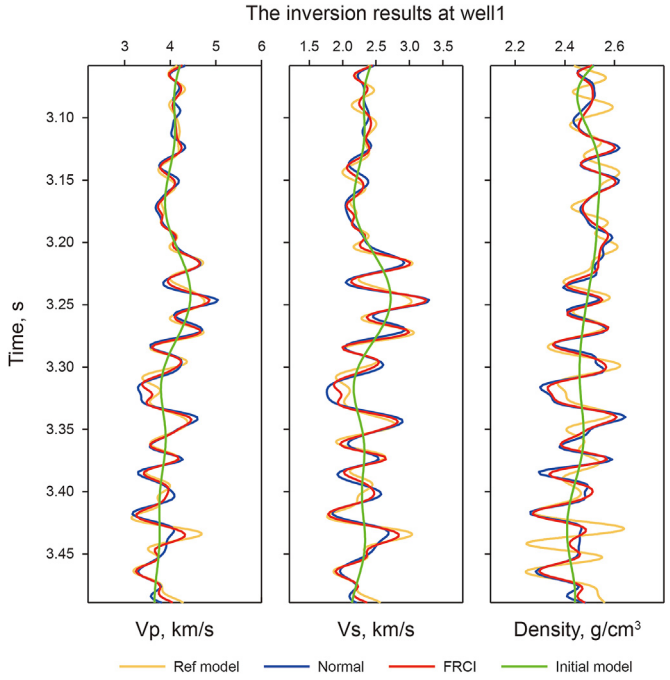


**Fig. 16.** The comparison between inversion results and logging curves at Well1. The blue and red lines are inversion results estimated by the conventional and proposed FRCI methods. The brown and green lines represent the reference and initial models, respectively. The reference model is obtained by filtering the logging curves to the seismic frequency band.

Yu (Yu et al., 2020) and Du (Du et al., 2018) set $w = 1$, we set $w = 2$ to suppress the noise of the synthetic and field seismic data. The selection of the neighborhood ranges is related to the stratum structure. A complex structure or high dip angles may require a larger neighborhood range. We test the effect of $\kappa$ on the inversion in the field data example. An ambiguous neighborhood range has little effect on the inversion results, which is consistent with Yu's study (Yu et al., 2020). In general, it is feasible to set $\kappa \in [-2\ 2]$ or $\kappa \in [-3\ 3]$ for the proposed approach. It is worth noting that the migration noise or residual moveout over- and under-correction can be detrimental to searching the shortest Euclidean distance. So some necessary processing is required before estimating the reflection features, or consider using the waveform features such as cross-correlation to reduce the uncertainty.

The regularization parameters $\lambda, \alpha > 0$ and the step size of iteration $\zeta$ need to be paid attention to when implementing the FRCI algorithm. We test the weight of the regularization term parallel to the reflection features $\lambda$ on the inversion results (Fig. 8). It is related to the lateral continuity, and a larger $\lambda$ can result in a more continuous model. However, a too large $\lambda$ may cause the model to be too smooth. The weight of the regularization term perpendicular to the reflection features $\alpha$ is related to the resolution. A small $\alpha$ may lead to spurious layers in the inversion results, or even non-convergence. $\zeta$ controls the convergence efficiency and accuracy of the FRCI algorithm. The larger $\zeta$ is, the faster the algorithm implements, and the larger the errors may be. If $\zeta$ is too small, the FRCI may not converge. Therefore, we'd better set a relatively large $\zeta$ first when debugging the parameters. Then, debug $\lambda$ and $\alpha$ according to their effect on the inversion results. Finally, an appropriately smaller $\zeta$ can be set to improve the accuracy of the inversion.

## 8. Conclusion

We propose an FRCI algorithm to achieve fast pre-stack seismic multi-channel inversion with reflection features constraints. The FRCI algorithm decomposes the estimated reflection features and re-characterizes them. Then, the introduction of reflection features adopts a new way, the Hadamard product operators, instead of the traditional seismic trace rearrangement strategy, which is disadvantageous for computation. This way liberates the memory and calculation of the computer and dramatically improves the efficiency of the inversion. Moreover, we derive a fast process for solving the objective function based on ADMM optimization. The Overthrust model and field data sets demonstrate the effectiveness of the proposed FRCI algorithm. This efficient algorithm may advance the broad application of multi-channel inversion in 3D seismic data.

## Declaration of competing interest

We declare that we do not have any commercial or associative

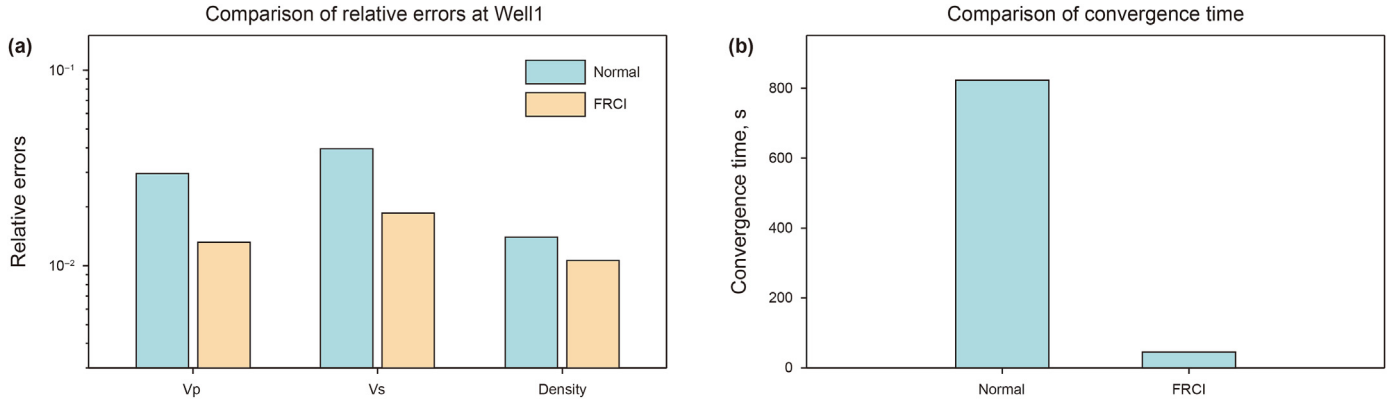


**Fig. 17.** (a) The comparison of relative errors between the logging curves and inversion results estimated by the conventional reflection features constrained inversion and FRCI at well1. (b) Comparison of the time taken to complete the inversion constrained by reflection features.

interest that represents a conflict of interest in connection with the work submitted.

## Acknowledgements

We would like to acknowledge the sponsorship of the National Natural Science Foundation of China (42004092, 42030103, 41974119), Marine S&T Fund of Shandong Province for Pilot National Laboratory for Marine Science and Technology (Qingdao) (Grant No.2021QNLM020001-6) and Young Elite Scientists Sponsorship Program by CAST (2021QNRC001).

## Appendix A

The objective function of FRCI (Eq. (27)) has been transformed into an augmented Lagrangian form (Eq. (29)) through the ADMM optimization. Alternately updating the variables can gradually approach the optimal solution through several iterations, and the update rules are as follows:

$$\mathbf{m}^{k+1} := \operatorname{argmin}\left\{\left\|\mathbf{S}-\mathbf{G}\mathbf{m}^{k}\right\|_{\mathrm{F}}^{2}+(\zeta/2)\left(\left\|\mathbf{m}^{k}\mathbf{R}_{x}-\mathbf{X}_{1}^{k}+\mathbf{Z}_{1}^{k}/\zeta\right\|_{\mathrm{F}}^{2}\right.\right.$$
$$+\left\|\mathbf{m}^{k}\mathbf{R}_{x}'-\mathbf{X}_{1}'^{k}+\mathbf{Z}_{1}'^{k}/\zeta\right\|_{\mathrm{F}}^{2}\Big)+(\zeta/2)\Big(\left\|\mathbf{R}_{z}\mathbf{m}^{k}-\mathbf{X}_{2}^{k}+\mathbf{Z}_{2}^{k}/\zeta\right\|_{\mathrm{F}}^{2}$$
$$\left.\left.+\left\|\mathbf{R}_{z}'\mathbf{m}^{k}-\mathbf{X}_{2}'^{k}+\mathbf{Z}_{2}'^{k}/\zeta\right\|_{\mathrm{F}}^{2}\Big)\right\}$$

$$\mathbf{X}_{1}^{k+1} := \operatorname{argmin}\left\{\lambda\left\|\mathbf{X}_{1}^{k+1}+\mathbf{H}_{1}\circ\mathbf{X}_{2}^{k}+\mathbf{H}_{2}\circ\mathbf{X}_{2}'^{k}\right\|_{\mathrm{F}}^{2}+\alpha\left\|\mathbf{X}_{2}^{k}-\mathbf{H}_{1}\right.\right.$$
$$\left.\left.\circ\mathbf{X}_{1}^{k+1}-\mathbf{H}_{2}\circ\mathbf{X}_{1}'^{k}\right\|_{\mathrm{F}}^{2}\quad+(\zeta/2)\left\|\mathbf{m}\mathbf{R}_{x}-\mathbf{X}_{1}^{k+1}+\mathbf{Z}_{1}^{k}/\zeta\right\|_{\mathrm{F}}^{2}\right\}$$

$$\mathbf{X}_{1}'^{k+1} := \operatorname{argmin}\left\{\alpha\left\|\mathbf{X}_{2}^{k}-\mathbf{H}_{1}\circ\mathbf{X}_{1}^{k+1}-\mathbf{H}_{2}\circ\mathbf{X}_{1}'^{k}\right\|_{\mathrm{F}}^{2}\right.$$
$$\left.+(\zeta/2)\left\|\mathbf{m}^{k+1}\mathbf{R}_{x}'-\mathbf{X}_{1}'^{k}+\mathbf{Z}_{1}'^{k}/\zeta\right\|_{\mathrm{F}}^{2}\right\}$$

$$\mathbf{X}_{2}^{k+1} := \operatorname{argmin}\left\{\lambda\left\|\mathbf{X}_{1}^{k+1}+\mathbf{H}_{1}\circ\mathbf{X}_{2}^{k}+\mathbf{H}_{2}\circ\mathbf{X}_{2}'^{k}\right\|_{\mathrm{F}}^{2}+\alpha\left\|\mathbf{X}_{2}^{k}\right.\right.$$
$$\left.\left.-\mathbf{H}_{1}\circ\mathbf{X}_{1}^{k+1}-\mathbf{H}_{2}\circ\mathbf{X}_{1}'^{k+1}\right\|_{\mathrm{F}}^{2}+(\zeta/2)\left\|\mathbf{m}^{k+1}\mathbf{R}_{z}-\mathbf{X}_{2}^{k}+\mathbf{Z}_{2}^{k}/\zeta\right\|_{\mathrm{F}}^{2}\right\}$$

$$\mathbf{X}_{2}'^{k+1} := \operatorname{argmin}\left\{\lambda\left\|\mathbf{X}_{1}^{k+1}+\mathbf{H}_{1}\circ\mathbf{X}_{2}^{k+1}+\mathbf{H}_{2}\circ\mathbf{X}_{2}'^{k+1}\right\|_{\mathrm{F}}^{2}\right.$$
$$\left.+(\zeta/2)\left\|\mathbf{R}_{z}'\mathbf{m}^{k+1}-\mathbf{X}_{2}'^{k}+\mathbf{Z}_{2}'^{k}/\zeta\right\|_{\mathrm{F}}^{2}\right\}$$

$$\mathbf{Z}_{1}^{k+1} := \operatorname{argmin}\left\{\mathbf{Z}_{1}^{k}+\zeta\left(\mathbf{m}^{k+1}\mathbf{R}_{x}-\mathbf{X}_{1}^{k+1}\right)\right\}$$

$$\mathbf{Z}_{1}'^{k+1} := \operatorname{argmin}\left\{\mathbf{Z}_{1}'^{k}+\zeta\left(\mathbf{m}^{k+1}\mathbf{R}_{x}'-\mathbf{X}_{1}'^{k+1}\right)\right\}$$

$$\mathbf{Z}_{2}^{k+1} := \operatorname{argmin}\left\{\mathbf{Z}_{2}^{k}+\zeta\left(\mathbf{R}_{z}\mathbf{m}^{k+1}-\mathbf{X}_{2}^{k+1}\right)\right\}$$

$$\mathbf{Z}_{2}'^{k+1} := \operatorname{argmin}\left\{\mathbf{Z}_{2}'^{k}+\zeta\left(\mathbf{R}_{z}'\mathbf{m}^{k+1}-\mathbf{X}_{2}'^{k+1}\right)\right\} \tag{A-1}$$

where **m**-minimization is a convex optimization with Frobenius norm regularization, the most common approach is to consider its partial derivative to be 1, and the partial derivative can be expressed as:

$$\frac{\partial f(\mathbf{m})}{\partial \mathbf{m}}=2\mathbf{G}^{\mathrm{T}}(\mathbf{G}\mathbf{m}-\mathbf{S})+(\zeta\mathbf{m}\mathbf{R}_{x}-\zeta\mathbf{X}_{1}+\mathbf{Z}_{1})\mathbf{R}_{x}^{\mathrm{T}}$$
$$+(\zeta\mathbf{m}\mathbf{R}_{x}'-\zeta\mathbf{X}_{1}'+\mathbf{Z}_{1}')\mathbf{R}_{x}'^{\mathrm{T}}+\mathbf{R}_{z}^{\mathrm{T}}(\zeta\mathbf{R}_{z}\mathbf{m}-\zeta\mathbf{X}_{2}+\mathbf{Z}_{2})$$
$$+\mathbf{R}_{z}'^{\mathrm{T}}(\zeta\mathbf{R}_{z}'\mathbf{m}-\zeta\mathbf{X}_{2}'+\mathbf{Z}_{2}') \tag{A-2}$$

Let $\frac{\partial f(\mathbf{m})}{\partial \mathbf{m}}=1$, Equation (A-2) can be simplified as follows:

$$(2\mathbf{G}^{\mathrm{T}}\mathbf{G}+\zeta\mathbf{R}_{z}^{\mathrm{T}}\mathbf{R}_{z}+\zeta\mathbf{R}_{z}'^{\mathrm{T}}\mathbf{R}_{z}')\mathbf{m}+\mathbf{m}(\zeta\mathbf{R}_{x}\mathbf{R}_{x}^{\mathrm{T}}+\zeta\mathbf{R}_{x}'\mathbf{R}_{x}'^{\mathrm{T}})$$
$$=2\mathbf{G}^{\mathrm{T}}\mathbf{S}+(\zeta\mathbf{X}_{1}-\mathbf{Z}_{1})\mathbf{R}_{x}^{\mathrm{T}}+(\zeta\mathbf{X}_{1}'-\mathbf{Z}')\mathbf{R}_{x}'^{\mathrm{T}}+\mathbf{R}_{z}^{\mathrm{T}}(\zeta\mathbf{X}_{2}-\mathbf{Z}_{2})$$
$$+\mathbf{R}_{z}'^{\mathrm{T}}(\zeta\mathbf{X}_{2}'-\mathbf{Z}_{2}') \tag{A-3}$$

Equation (A-3) can be solved by eigenvalue decomposition because it is a standard Sylvester equation $\mathbf{A}\mathbf{m}+\mathbf{m}\mathbf{B}=\mathbf{C}$, where

$$\mathbf{A}=2\mathbf{G}^{\mathrm{T}}\mathbf{G}+\zeta\mathbf{R}_{z}^{\mathrm{T}}\mathbf{R}_{z}+\zeta\mathbf{R}_{z}'^{\mathrm{T}}\mathbf{R}_{z}'$$
$$\mathbf{B}=\zeta\mathbf{R}_{x}\mathbf{R}_{x}^{\mathrm{T}}+\zeta\mathbf{R}_{x}'\mathbf{R}_{x}'^{\mathrm{T}}$$
$$\mathbf{C}=2\mathbf{G}^{\mathrm{T}}\mathbf{S}+(\zeta\mathbf{X}_{1}-\mathbf{Z}_{1})\mathbf{R}_{x}^{\mathrm{T}}+(\zeta\mathbf{X}_{1}'-\mathbf{Z}')\mathbf{R}_{x}'^{\mathrm{T}}+\mathbf{R}_{z}^{\mathrm{T}}(\zeta\mathbf{X}_{2}-\mathbf{Z}_{2})$$
$$+\mathbf{R}_{z}'^{\mathrm{T}}(\zeta\mathbf{X}_{2}'-\mathbf{Z}_{2}') \tag{A-4}$$

The $\mathbf{X}_1$-, $\mathbf{X}_1'$-, $\mathbf{X}_2'$-, and $\mathbf{X}_2'$-minimization is tricky because the Hadamard product operator exacerbates the complexity of the equation derivation. First, we derive the partial derivatives of a

simple formula $\|\mathbf{A}\circ\mathbf{X}+\mathbf{B}\|_{\mathrm{F}}^2$. According to the definition of Frobenius norm, we have:

$$\begin{aligned}&\|\mathbf{A}\circ\mathbf{X}+\mathbf{B}\|_{\mathrm{F}}^2=Tr((\mathbf{A}\circ\mathbf{X}+\mathbf{B})^{\mathrm{T}}(\mathbf{A}\circ\mathbf{X}+\mathbf{B}))\\&=Tr((\mathbf{A}\circ\mathbf{X})^{\mathrm{T}}(\mathbf{A}\circ\mathbf{X})+(\mathbf{A}\circ\mathbf{X})^{\mathrm{T}}\mathbf{B}+\mathbf{B}^{\mathrm{T}}(\mathbf{A}\circ\mathbf{X})+\mathbf{B}^{\mathrm{T}}\mathbf{B})\end{aligned}\tag{A-5}$$

where $Tr$ is the sum of the diagonal elements of a matrix. $(\mathbf{A}\circ\mathbf{X})^{\mathrm{T}}\mathbf{B}$ at a certain point is $[(\mathbf{A}\circ\mathbf{X})^{\mathrm{T}}\mathbf{B}]_{i,j}=\sum_{p=1}^{m}(\mathbf{A}_{pi}\mathbf{X}_{pi})\mathbf{B}_{pj}$. Let $i=j=s$, the term of $Tr((\mathbf{A}\circ\mathbf{X})^{\mathrm{T}}\mathbf{B})$ can be expressed as follows:

$$Tr((\mathbf{A}\circ\mathbf{X})^{\mathrm{T}}\mathbf{B})=\sum_{s=1}^{n}\sum_{p=1}^{m}\mathbf{A}_{ps}\mathbf{X}_{ps}\mathbf{B}_{ps}\tag{A-6}$$

Let $p=i$ and $s=j$, the partial derivative of $Tr((\mathbf{A}\circ\mathbf{X})^{\mathrm{T}}\mathbf{B})$ with respect to $\mathbf{X}$ can be expressed as:

$$[\partial Tr((\mathbf{A}\circ\mathbf{X})^{\mathrm{T}}\mathbf{B})/\partial\mathbf{X}]_{ij}=\frac{\partial(\mathbf{A}_{ij}\mathbf{X}_{ij}\mathbf{B}_{ij})}{\partial\mathbf{X}_{ij}}=[\mathbf{A}\circ\mathbf{B}]_{ij}\tag{A-7}$$

Similarly,

$$\begin{aligned}&\partial Tr(\mathbf{B}^{\mathrm{T}}(\mathbf{A}\circ\mathbf{X}))/\partial\mathbf{X}=\mathbf{A}\circ\mathbf{B}\\&\partial Tr((\mathbf{A}\circ\mathbf{X})^{\mathrm{T}}(\mathbf{A}\circ\mathbf{X}))/\partial\mathbf{X}=2\mathbf{A}\circ\mathbf{A}\circ\mathbf{B}\end{aligned}\tag{A-8}$$

Therefore,

$$\partial\|\mathbf{A}\circ\mathbf{X}+\mathbf{B}\|_{\mathrm{F}}^2\Big/\partial\mathbf{X}=2(\mathbf{A}\circ\mathbf{A}\circ\mathbf{X}+\mathbf{A}\circ\mathbf{B})\tag{A-9}$$

For the $\mathbf{X}_1$-minimization, the partial derivative of the formula with respect to $\mathbf{X}_1$ can be expressed as follows:

$$\begin{aligned}\frac{\partial f(\mathbf{X}_1)}{\partial\mathbf{X}_1}=&2\lambda(\mathbf{X}_1+\mathbf{H}_1\circ\mathbf{X}_2+\mathbf{H}_2\circ\mathbf{X}_2')+2\alpha\mathbf{H}_1\circ\\&(\mathbf{H}_1\circ\mathbf{X}_1+\mathbf{H}_2\circ\mathbf{X}_1'-\mathbf{X}_2)+(\zeta\mathbf{X}_1-\zeta\mathbf{m}\mathbf{R}_x-\mathbf{Z}_1)\end{aligned}\tag{A-10}$$

let $\frac{\partial f(\mathbf{X}_1)}{\partial\mathbf{X}_1}=0$, we can obtain the following equation:

$$\begin{aligned}&(2\alpha\mathbf{H}_1\mathbf{H}_1+\zeta+2\lambda)\mathbf{X}_1=2\alpha\mathbf{H}_1(\mathbf{X}_2-\mathbf{H}_2\circ\mathbf{X}_1')+\zeta\mathbf{m}\mathbf{R}_x+\mathbf{Z}_1\\&-2\lambda(\mathbf{H}_1\circ\mathbf{X}_2+\mathbf{H}_2\circ\mathbf{X}_2')\end{aligned}\tag{A-11}$$

Based on the definition of Hadamard product operator, the solution of $\mathbf{X}_1$ can be obtained as follows:

$$\begin{aligned}\mathbf{X}_1=&\big(2\alpha\mathbf{H}_1\circ(\mathbf{X}_2-\mathbf{H}_2\circ\mathbf{X}_1')+\zeta\mathbf{m}\mathbf{R}_x+\mathbf{Z}_1\\&-2\lambda(\mathbf{H}_1\circ\mathbf{X}_2+\mathbf{H}_2\circ\mathbf{X}_2')\big)/(2\alpha\mathbf{H}_1\circ\mathbf{H}_1+\zeta+2\lambda)\end{aligned}\tag{A-12}$$

Similarly, we derive the minimization of $\mathbf{X}_1$, $\mathbf{X}_1$, and $\mathbf{X}_1$ as follows:

$$\begin{cases}\mathbf{X}_1'=(\zeta\mathbf{m}\mathbf{R}_x'+\mathbf{Z}_1'+2\alpha\mathbf{H}_2\circ(\mathbf{X}_2-\mathbf{H}_1\circ\mathbf{X}_1))./(2\alpha\mathbf{H}_2\circ\mathbf{H}_2+\zeta)\\\mathbf{X}_2=(\zeta\mathbf{R}_z\mathbf{m}+\mathbf{Z}_2-2\lambda\mathbf{H}_1\circ(\mathbf{X}_1+\mathbf{H}_2\circ\mathbf{X}_2')+2\alpha(\mathbf{H}_1\circ\mathbf{X}_1+\mathbf{H}_2\circ\mathbf{X}_1'))\\\quad./(2\lambda\mathbf{H}_1\circ\mathbf{H}_1+2\alpha+\zeta)\\\mathbf{X}_2'=(\zeta\mathbf{R}_z'\mathbf{m}+\mathbf{Z}_2'-2\lambda\mathbf{H}_2\circ(\mathbf{X}_1+\mathbf{H}_1\circ\mathbf{X}_2))./(2\lambda\mathbf{H}_2\circ\mathbf{H}_2+\zeta)\end{cases}\tag{A-13}$$

where ./ is the right array division operation, denoting the element-by-element division of two matrices with the same size. The update of the dual variables $\mathbf{Z}_1$, $\mathbf{Z}_2$, $\mathbf{Z}_1'$, and $\mathbf{Z}_2'$ can be expressed as:

$$\begin{cases}\mathbf{Z}_1=\mathbf{Z}_1+\zeta(\mathbf{m}\mathbf{R}_x-\mathbf{X}_1)\\\mathbf{Z}_1'=\mathbf{Z}_1'+\zeta(\mathbf{m}\mathbf{R}_x'-\mathbf{X}_1')\\\mathbf{Z}_2=\mathbf{Z}_2+\zeta(\mathbf{R}_z\mathbf{m}-\mathbf{X}_2)\\\mathbf{Z}_2'=\mathbf{Z}_2'+\zeta(\mathbf{R}_z'\mathbf{m}-\mathbf{X}_2')\end{cases}\tag{A-14}$$

## References


Abma, R., Claerbout, J., 1995. Lateral prediction for noise attenuation by t-x and f-x techniques. Geophysics 60 (6), 1887–1896. https://doi.org/10.1190/1.1443920.

Aki, K., Richards, P.G., 1980. Quantitative Seismology: Theory and Methods. W.H. Freeman and Co., New York.

Bai, M., Chen, W., Chen, Y.K., 2019. Nonstationary least-squares decomposition with structural constraint for denoising multi-channel seismic data. IEEE Trans. Geosci. Rem. Sens. 57 (12), 10437–10446. https://doi.org/10.1109/TGRS.2019.2935799.

Bertsekas, D.P., 1999. Nonlinear Programming, second ed. Athena Scientific.

Boyd, S., Parikh, N., Chu, E., et al., 2010. Distributed optimization and statistical learning via the alternating direction method of multipliers. Mach. Learn. 3 (1), 1–122. https://doi.org/10.1561/2200000016.

Cheng, L., Wang, S.X., Wei, W.W., et al., 2020. Structural geosteering constrained multi-trace sparse reflectivity inversion based on mixed norms. J. Appl. Geophys. 172, 103880. https://doi.org/10.1016/j.jappgeo.2019.103880.

Du, X., Li, G.F., Zhang, M., et al., 2018. Multichannel band-controlled deconvolution based on a data-driven structural regularization. Geophysics 83 (5), R401–R411. https://doi.org/10.1190/geo2017-0516.1.

Gholami, A., 2016. A fast automatic multichannel blind seismic inversion for high-resolution impedance recovery. Geophysics 81 (5), V357–V364. https://doi.org/10.1190/geo2015-0654.1.

Gholami, A., 2015. Nonlinear multichannel impedance inversion by total-variation regularization. Geophysics 80 (5), R217–R224. https://doi.org/10.1190/geo2015-0004.1.

Gholami, A., Sacchi, M.D., 2013. Fast 3D blind seismic deconvolution via constrained total variation and GCV. SIAM J. Imag. Sci. 6 (4), 2350–2369. https://doi.org/10.1137/130905009.

Goodway, B., Chen, C.T.W., Jon, D., 1997. Improved AVO fluid detection and lithology discrimination using Lamé petrophysical parameters; "λρ,""μρ,"&"λ/μ fluid stack," from P and S inversions. In: SEG Tech. Progr. Expand. Abstr. https://doi.org/10.1190/1.1885795.

Gray, D., Andersen, E., 2000. Application of AVO and inversion to formation properties. World Oil 221 (7), 85–90.

Hamid, H., Pidlisecky, A., Lines, L., 2018. Prestack structurally constrained impedance inversion. Geophysics 83 (2), R89–R103. https://doi.org/10.1190/geo2016-0703.1.

Hamid, H., Pidlisecky, A., 2016. Structurally constrained impedance inversion. Interpretation 4 (4), T577–T589. https://doi.org/10.1190/INT-2016-0049.1.

Hamid, H., Pidlisecky, A., 2015. Multitrace impedance inversion with lateral constraints. Geophysics 80 (6), M101–M111. https://doi.org/10.1190/geo2014-0546.1.

Kazemi, N., Sacchi, M.D., 2014. Sparse multichannel blind deconvolution. Geophysics 79 (5), V143–V152. https://doi.org/10.1190/geo2013-0465.1.

Lee, J., Kim, G., Nam, H., et al., 2017. Based on block coordinate descent methods. The Journal of Korean Institute of Communications and Information Sciences 42 (7), 1509–1511. https://doi.org/10.7840/kics.2017.42.7.1509.

Li, K., Yin, X.Y., Zong, Z.Y., et al., 2021. Estimation of porosity, fluid bulk modulus, and stiff-pore volume fraction using a multitrace Bayesian amplitude-variation-with-offset petrophysics inversion in multiporosity reservoirs. Geophysics 87 (1), M25–M41. https://doi.org/10.1190/geo2021-0029.1.

Li, K., Yin, X.Y., Zong, Z.Y., et al., 2020. Seismic AVO statistical inversion incorporating poroelasticity. Petrol. Sci. 17 (3), 1237–1258. https://doi.org/10.1007/s12182-020-00483-5.

Li, S., Peng, Z.M., Wu, H., 2018. Prestack multi-gather simultaneous inversion of elastic parameters using multiple regularization constraints. J. Earth Sci. 29 (6), 1359–1371. https://doi.org/10.1007/s12583-017-0905-7.

Liu, G.C., Fomel, S., Jin, L., et al., 2009. Stacking seismic data using local correlation. Geophysics 74 (3), V43–V48. https://doi.org/10.1190/1.3085643.

Loan, C.F.V., 2000. The ubiquitous Kronecker product. J. Comput. Appl. Math. 123 (1), 85–100. https://doi.org/10.1016/S0377-0427(00)00393-9.

Ma, M., Zhang, R., Yuan, S.Y., 2018. Multichannel impedance inversion for nonstationary seismic data based on the modified alternating direction method of multipliers. Geophysics 84 (1), A1–A6. https://doi.org/10.1190/geo2018-0319.1.

Ma, X., Li, G.F., Li, H., et al., 2020. Multichannel absorption compensation with a data-driven structural regularization. Geophysics 85 (1), V71–V80. https://doi.org/10.1190/geo2019-0132.1.

Nose-Filho, K., Takahata, A.K., Lopes, R., et al., 2015. A fast algorithm for sparse multichannel blind deconvolution. Geophysics 81 (1), V7–V16. https://doi.org/10.1190/geo2015-0069.1.

Rimstad, K., Avseth, P., Omre, H., 2012. Hierarchical Bayesian lithology/prediction: a North Sea case study. Geophysics 77 (2), B39–B85. https://doi.org/10.1190/

geo2011-0202.1.
Smith, G.C., Gidlow, P.M., 1987. Weighted stacking for rock property estimation and detection of gas. Geophys. Prospect. 35 (9), 993–1014. https://doi.org/10.1111/j.1365-2478.1987.tb00856.x.
Sroubek, F., Milanfar, P., 2012. Robust multichannel blind deconvolution via fast alternating minimization. IEEE Trans. Image Process. 21 (4), 1687–1700. https://doi.org/10.1109/TIP.2011.2175740.
Wang, Y.J., Lin, W.C., San, C., et al., 2018. The fast seismic multitrace inversion based on adaptive mixed norm. In: SEG Global Meeting Abstr. https://doi.org/10.1190/IGC2018-292.
Wang, L.Q., Zhou, H., Liu, W.L., et al., 2021. Data-driven multichannel poststack seismic impedance inversion via patch-ordering regularization. Geophysics 86 (2), R197–R210. https://doi.org/10.1190/geo2020-0253.1.
Wang, L.Q., Zhou, H., Wang, Y.F., et al., 2019. Three-parameter prestack seismic inversion based on L1-2 minimization. Geophysics 84 (5), R753–R766. https://doi.org/10.1190/geo2018-0730.1.
Wright, S.J., 2015. Coordinate descent algorithms. Math. Program. 151 (1), 3–34. https://doi.org/10.1007/s10107-015-0892-3.
Xi, Y.J., Yin, X.Y., Liu, X.J., et al., 2022. Amplitude-variation-with-offset inversion based on group sparse regularization. Interpretation 10 (1). https://doi.org/10.1190/INT-2019-0132.1. SA1-SA14.
Yang, Y.M., Yin, X.Y., Li, K., et al., 2022. Data-driven fast prestack structurally constrained inversion. Geophysics 87 (3), N31–N43. https://doi.org/10.1190/geo2021-0145.1.
Yin, X.Y., Yang, Y.M., Li, K., et al., 2020. Multitrace inversion driven by cross-correlation of seismic data. Chin. J. Geophys. 63 (10), 3827–3837. https://doi.org/10.6038/cjg2020O0075 (in Chinese).
Yin, X.Y., Zong, Z.Y., Wu, G.C., 2015. Research on seismic fluid identification driven by rock physics. Sci. China Earth Sci. 58 (2), 159–171. https://doi.org/10.1007/s11430-014-4992-3.
Yu, B., Zhou, H., Wang, L.Q., et al., 2020. Prestack Bayesian statistical inversion constrained by reflection features. Geophysics 85 (4), R349–R363. https://doi.org/10.1190/geo2019-0810.1.
Yuan, S.Y., Wang, S.X., Nan, T., et al., 2015. Simultaneous multitrace impedance inversion with transform-domain sparsity promotion. Geophysics 80 (3), R71–R80. https://doi.org/10.1190/geo2014-0065.1.
Zhang, S.C., Fan, X., Li, G.F., 2019. Multi-trace blocky reflectivity inversion with anisotropic total variation regularization. In: SEG Technical Program Expanded Abstracts, pp. 590–594. https://doi.org/10.1190/segam2019-3215511.1.
Zhang, G.Z., Pan, X.P., Li, Z.Z., et al., 2015. Seismic fluid identification using a nonlinear elastic impedance inversion method based on a fast Markov chain Monte Carlo method. Petrol. Sci. 12 (3), 406–416. https://doi.org/10.1007/s12182-015-0046-5.
Zhang, R., Sen, M.K., Srinivasan, S., 2013a. A prestack basis pursuit seismic inversion. Geophysics 78 (1), R1–R11. https://doi.org/10.1190/geo2011-0502.1.
Zhang, R., Sen, M.K., Srinivasan, S., 2013b. Multi-trace basis pursuit inversion with spatial regularization. J. Geophys. Eng. 10, 035012. https://doi.org/10.1088/1742-2132/10/3/035012.
Zhang, Y.Y., Sun, S.Z.D., Yang, H.J., et al., 2011. Pre-stack inversion for caved carbonate reservoir prediction: a case study from Tarim Basin, China. Petrol. Sci. 8 (4), 415–421. https://doi.org/10.1007/s12182-011-0159-4.
Zhang, Z.D., Alkhalifah, T., 2019. Local-crosscorrelation elastic full-waveform inversion. Geophysics 84 (6), R897–R908. https://doi.org/10.1190/geo2018-0660.1.
Zong, Z.Y., Feng, Y.W., Yin, X.Y., et al., 2021. Fluid discrimination incorporating viscoelasticity and frequency-dependent amplitude variation with offsets inversion. Petrol. Sci. 18 (4), 1047–1058. https://doi.org/10.1016/j.petsci.2020.10.001.
Zong, Z.Y., Li, K., Yin, X.Y., et al., 2017. Broadband seismic amplitude variation with offset inversion. Geophysics 82 (3), M43–M53. https://doi.org/10.1190/geo2016-0306.1.
Zong, Z.Y., Yin, X.Y., Wu, G.C., 2015. Geofluid discrimination incorporating poroelasticity and seismic reflection inversion. Surv. Geophys. 36 (5), 659–681. https://doi.org/10.1007/s10712-015-9330-6.
Zong, Z.Y., Yin, X.Y., Wu, G.C., 2013. Elastic impedance parameterization and inversion with Young's modulus and Poisson's ratio. Geophysics 78 (6), N35–N42. https://doi.org/10.1190/geo2012-0529.1.